A Yolk-like Multifunctional Platform for Multimodal Imaging and Synergistic Therapy Triggered by a Single Near-Infrared Light

Ruichan Lv,[†] Piaoping Yang,[*,†] Fei He,[†] Shili Gai,[†] Chunxia Li,[‡] Yunlu Dai,[†] Guixin Yang,[†] and Jun Lin[*,‡]

[†]Key Laboratory of Superlight Materials and Surface Technology, Ministry of Education, College of Material Sciences and Chemical Engineering, Harbin Engineering University, Harbin 150001, P. R. China and [‡]State Key Laboratory of Rare Earth Resource Utilization, Changchun Institute of Applied Chemistry, Chinese Academy of Sciences, Harbin 130021, P. R. China

ABSTRACT To integrate photodynamic therapy (PDT) with photothermal therapy (PTT) and chemotherapy for enhanced antitumor efficiency, we developed a mild and rational route to synthesize novel multifunctional GdOF:Ln@SiO_2 (Ln = 10%Yb/1% Er/4%Mn) mesoporous capsules using strong up-conversion luminescent (UCL) GdOF:Ln as cores and mesoporous silica layer as shells, followed by modification with varied functional groups onto the framework. It was found that due to the codoped Yb/Er/Mn in GdOF, the markedly enhanced red emission can efficiently transfer energy to the conjugated PDT agent (ZnPc) which produces high singlet oxygen, and the incorporated carbon dots outside the shell can generate obvious thermal effect under 980 nm laser irradiation and also prevent the premature leaking of ZnPc. Simultaneously, the as-produced thermal effect can obviously enhance the doxorubicin (DOX) release, which greatly improves the chemotherapy, resulting in a synergistic therapeutic effect. The system exhibits drastically enhanced therapeutic efficiency against tumor growth, as demonstrated both *in vitro* and *in vivo*. Especially, the doped rare earth ions in the host endow the material with excellent UCL imaging, magnetic resonance imaging (MRI), and computed tomography (CT) imaging properties, thus realizing the target of multimodal imaging guided multiple therapies.

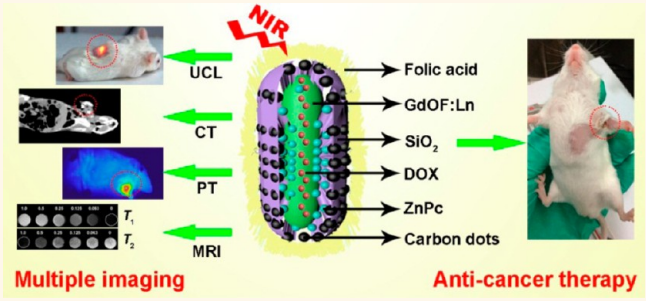

KEYWORDS: photodynamic therapy · photothermal therapy · bioimaging · up-conversion · GdOF

In recent years, because most of anticancer drugs may have strong toxicity and side-effect with a large dosage, researchers have focused on synthesizing the functional materials with special structure in order to encapsulate diverse functional groups and particles, such as anticancer drugs, photothermal therapy (PTT) and photodynamic therapy (PDT) photosensitizers (PSs) onto the carriers, in order to control the release process or achieve the targeted therapy without damage to normal organs.[1−9] Up to now, a large number of functional structures have been utilized as main drug-carriers in the drug delivery systems (DDSs). Among them, silica-based functional materials have especially been applied as effective carriers for DDSs due to their mesoporous structure, large surface area, tunable pore size, optical transparency, and facile surface modification.[10−15] In the field of material synthesis, most of the core/shell and hollow structures are spheres which are facile to obtain. However, the elliptical capsules with high length-diameter ratio which may have different endocytosis,[16,17] are relatively less reported, especially for yolk-like core−shell structures.

To the DDSs, if referred to image-guided PDT and PTT, two separate lights with different wavelengths were often adopted to realize imaging and therapy which makes it difficult for real-time monitoring and efficacy assessment. Therefore, near-infrared (NIR) excitation at 980 nm is potentially used as the up-conversion emissions because UCL emissions in visible regions could be

* Address correspondence to yangpiaoping@hrbeu.edu.cn, jlin@ciac.ac.cn.

Received for review November 7, 2014 and accepted January 12, 2015.

Published online January 12, 2015
10.1021/nn5063613

utilized as the donors for transferring energy to PDT or PTT agents.[18−23] Meanwhile, NIR laser located within the optical transmission window of biological specimens has the merits of high detection sensitivity, large penetration depth, increased image contrast, and decreased damage to cells,[24−29] which are importantly utilized for biological cells and living organisms.[30−36] Lanthanide oxyfluorides (LnOF) have been considered as excellent luminescent host materials for achieving efficient up-conversion luminescent properties, which are even better than lanthanide fluoride.[37,38] In particular, Gd^{3+} ions can play an effective role as the intermediate sublattice in enhancing the doped activators efficiency, and Gd^{3+}/Yb^{3+} doped particles have been proved excellent CT contrast agents due to the high atomic and strong X-ray attenuation.[39,40] Meanwhile, Gd-based UCL particles can be used as contrast agents for MRI due to their unpaired 4f electrons.[41,42] However, most of the researchers focus on LnOF bulk crystals or regular particles prepared by some limited chemical routes,[43,44] and there is no literature on the GdOF particles with functional structure for biomedical application.

For a secure and efficient PDT, it requires high $^1O_2$ quantum yield, short irradiation time, and low irradiation pump power (<0.7 W/cm^2).[45,46] The $^1O_2$ production in the UCL system is dependent on the spectral overlap between the donor and acceptor, the distance between the two counterparts and the quantity of PSs loaded. Thus, it is important to design the UCL host/dopant and material structure. As an effective UCL material, Yb^{3+}/Er^{3+}, Yb^{3+}/Ho^{3+}, and Yb^{3+}/Tm^{3+} have been proposed as efficient NIR-to-visible dopant as the bioimaging and optical carrier.[47−51] The multiple emission regions can provide wide choice for different PDT agents. Meanwhile, the strong red UCL of Yb^{3+} codoped is desirable for the biological/biomedical applications because that the green light is shallowly penetrated depth and the red emission signal is easier to be detected. Nowadays, researchers have made attempt to obtain higher red-to-green (R/G) emissions by increasing the concentration of Yb^{3+} in Yb^{3+}/Er^{3+} codopant due to the cross-relaxation of Er^{3+} → Er^{3+}.[52] However, the excess dopants in the host lattice would decrease Yb^{3+} → Er^{3+} interatomic distance and thus facilitate back-energy-transfer from Er^{3+} to Yb^{3+}, resulting in the decreased up-conversion (UC) emission.[53,54] Thus, it is still a challenge to rationally control the two emissions output in order to effectively enhance the R/G emission which is important for their bioimaging penetration depth.[55−57]

In this work, we propose a novel strategy to prepare multifunctional GdOF:Ln@SiO_2 yolk-like microcapsules using UCL GdOF:Ln as core, mesoporous silica as shell and large hollow cavities between the core and shell, then applied as both multiple imaging (CT, MRI, UCL, photothermal) agent and drug carriers for multiple anticancer therapy (PDT, PTT, and chemo-). Zinc(II)-phthalocyanine (ZnPc) PSs were modified to endow GdOF:Ln@SiO_2 with ability to product singlet oxygen ($^1O_2$) when excited by red emission derived from NIR irradiation, and the attached carbon dots are to generate thermal effect under NIR laser irradiation. Simultaneously, the produced thermal effect induced enhanced DOX release is to generate a synergistic therapeutic effect. Moreover, the MRI, X-ray CT together with the UCL imaging *in vitro* and *in vivo* were employed to investigate the imaging properties. The biocompatibility, the drug loading and release, the cytotoxicity to HeLa cells *in vitro*, the anti-H22 tumor therapy *in vivo* and the histologic section analysis were investigated as well.

RESULTS AND DISCUSSION

Synthesis and Characterization of UCMCs. XRD patterns of the products prepared at different synthetic steps are presented in Supporting Information Figure S1. No obvious diffraction peaks can be observed for the precursor and carbon and silica coated sample, which indicates the two samples are amorphous. After calcination, the well-defined diffraction peaks of the product can be directly indexed to rhombohedral GdOF (JCPDS No. 50-0569). Meanwhile, the wide diffraction peaks and low intensity suggest the nanosized nature of the crystallites that form the product, which was calculated to be 8.9 nm by the Scherrer formula. In addition, the cell lattice parameters a = 3.8597 Å and c = 19.092 Å match well with undoped GdOF (a = 3.865 Å and c = 19.258 Å). The slight contraction of the parameters is due to the smaller ionic radius of the dopant ions substituting for the larger Gd^{3+} ions. Considering the little difference about the phases between up-doped GdOF and GdOF:Ln, here GdOF:10%Yb/1%Er/4%Mn (referred to as GdOF:Ln) was chosen as the typical sample for the following discussion.

Scheme 1a illustrates the formation process of GdOF:Ln mesoporous capsules, and the SEM images, TEM images and morphology sketches of the products obtained at different steps are shown in Figure 1. The SEM and low-magnified TEM images reveal that the samples are mainly composed of a large number of well-dispersed ellipsoids. In Figure 1a1-a4, the average size of the precursor is about 180 nm in width and 430 nm in length. After coating a layer of C with an average thickness of 30 nm, the as-obtained $Gd(OH)_x$-$(CO_3)_yF_z$:Ln@C has a mean width of about 240 nm and length of 460 nm. As shown in Figure 1b1−b4, the C layer is smooth with uniform thickness, which plays a significant role in keeping the shape of the ellipsoid and makes a good foundation for next coating of silica. After that, a thinner layer of mesoporous SiO_2 (with an average thickness of 30 nm) was deposited on carbon

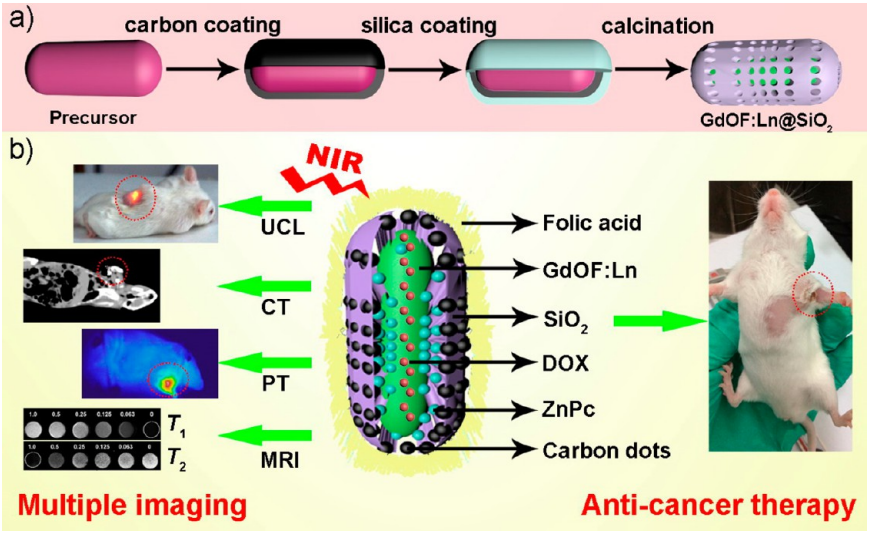

Scheme 1. Schematic illustration for the synthesis of GdOF:Ln@SiO_2−ZnPc-CDs microcapsule and bio-application for multiple imaging and anti-tumor therapy.

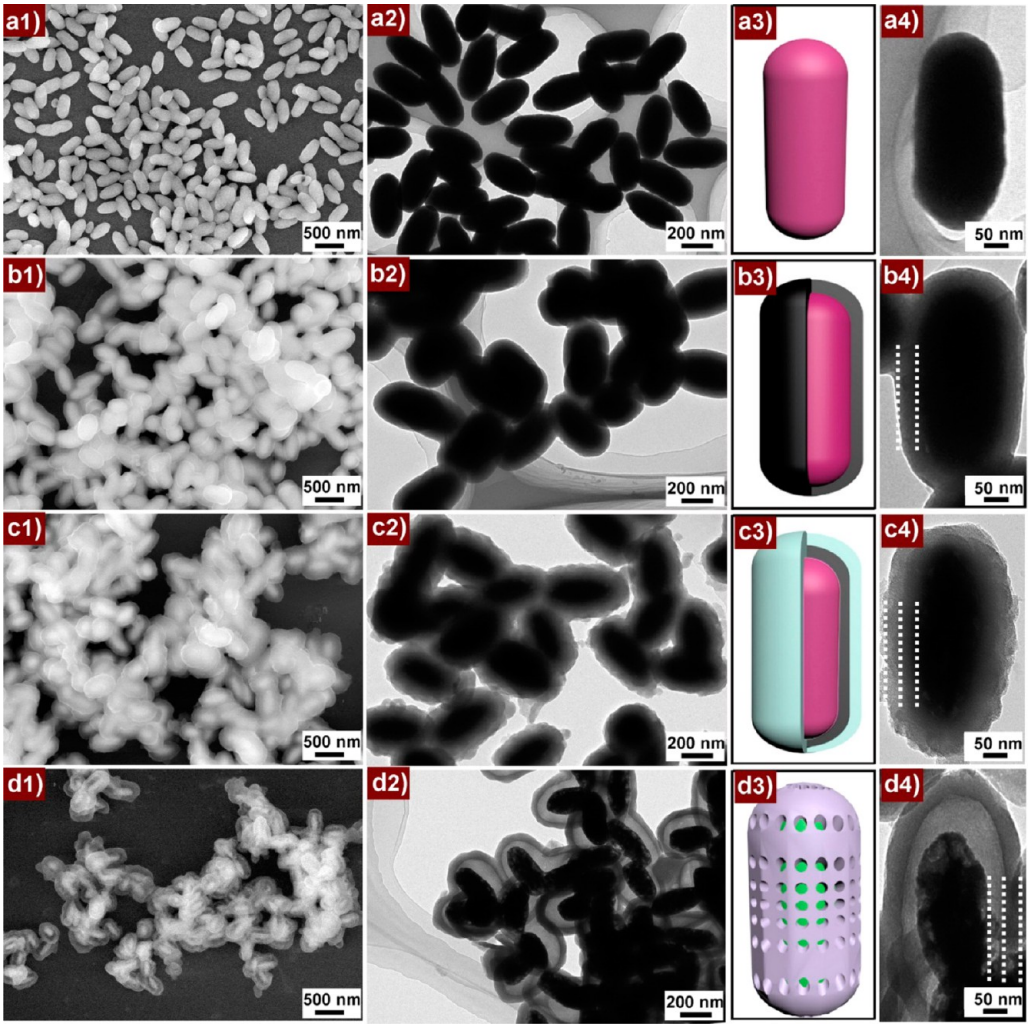

Figure 1. SEM images, TEM images, and morphology sketches of (a1−a4) $Gd(OH)_x(CO_3)_yF_z$:Ln, (b1−b4) $Gd(OH)_x(CO_3)_yF_z$:Ln@C, (c1−c4) $Gd(OH)_x(CO_3)_yF_z$:Ln@C@mSiO_2, and (d1−d4) GdOF:Ln@SiO_2.

layer surface due to the interaction of C and silica. The average size of $Gd(OH)_x(CO_3)_yF_z$:Ln@C@SiO_2 is about 280 nm in width and 500 nm in length (Figure 1c1−c4). The decreased length/width ratio may be attributed to

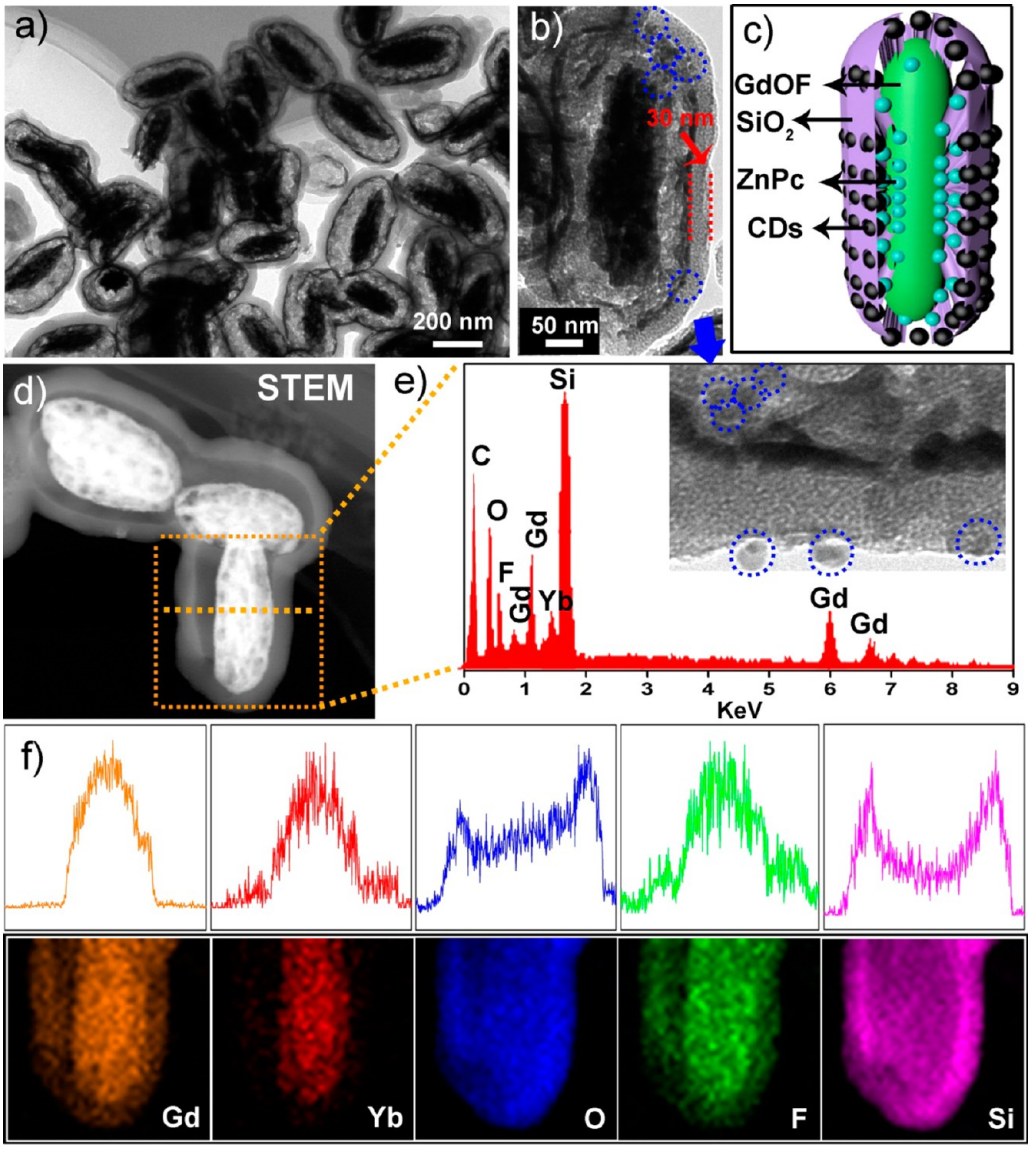

Figure 2. (a and b) TEM images with different magnification, (c) morphology sketch, (d) STEM image, (e) EDS, and (F) the cross-sectional compositional line profiles and elemental mapping images of GdOF:Ln@mSiO$_2$−ZnPC-CDs.

the different attraction of the diverse surface areas. Finally, GdOF:Ln@SiO_2 yolk-like submicrocapsules have been prepared after calcination (Figure 1d1-d4). The cores are generated due to the shrink of $Gd(OH)_x(CO_3)_yF_z$:Ln to GdOF:Ln during the annealing process. The mesoporous SiO_2 outside shell is derived from the removal of CTAB. The large cavity between the inside core and the outside shell is formed due to the burning of C layer.

The mesoporous pores of the microcapsules provide the probability to modify or store functional groups and nanoparticles. After modified with amino groups, the as-obtained GdOF:Ln@SiO_2−NH_2 particles are conjugated with ZnPc PSs. Then, the carbon dots (CDs) are decorated on the surface, which were synthesized by cutting the nanotubes using the mixture of HNO_3 and H_2SO_4 under water reflux. TEM images of carbon nanotubes and carbon dots are shown in Supporting Information Figure S2. The CDs are highly dispersed with an average size of 2−7 nm (Supporting Information Figure S2b). From the photographs of nanotubes and CDs dispersed in the PBS solution, we can see the CDs solution is clearly brown with high particle dispersion, instead of large nanotube particles deposited at the bottom. As a PTT agent, CDs can effectively absorb the NIR light and then convert to thermal effect. Meanwhile, well-dispersed CDs inside the mesoporous channels of silica may also effectively prevent the leaching of ZnPc PSs. After functionalized with FA, the final GdOF:Ln@SiO_2−ZnPc-CDs-FA UCL microcapsules (UCMCs) have been synthesized, which are illustrated by the TEM image (Figure 2a,b) and shape sketch (Figure 2c). As shown, the microcapsules are well dispersed with clear GdOF:Ln cores and silica shell. From the magnified TEM image, the carbon dots can be apparently found. The STEM image (Figure 2d)

and energy dispersive spectrometer (EDS) (Figure 2e) prove that there are Gd, Yb, O, F, Si, and C elements in the as-prepared sample. The elemental line and mapping images (Figure 2e) further confirm the yolk-like structure and the uniform dispersion of the elements. We also performed the DLS measurement of UCMCs which is given in Supporting Information Figure S3. As shown, the average size is 293.0 nm with a relatively narrow distribution.

In the FT-IR spectra (Supporting Information Figure S4), a similar band in all four samples at 3345 cm^{-1} is due to the −OH stretching and bending vibrations of water. This strong absorption band indicates a large number of −OH groups present on the surface, which are important for bonding functional groups. For $Gd(OH)_x(CO_3)_yF_z$:Ln precursor (Supporting Information Figure S3a), the characteristic absorption bands of O−C−O (1523 and 1401 cm^{-1}), −OH (1082 cm^{-1}), π-CO_3^{2-} (843 cm^{-1}), and δ-CO_3^{2-} (753 cm^{-1}, 688 cm^{-1}) indicate the existence of −OH and CO_3^{2-} (Supporting Information Figure S4a).[58] After coating C layer, the −C═C (1620 cm^{-1}) and −C−OH (1270 cm^{-1}) bands are due to the hydrolysis of glucose (Supporting Information Figure S4b,c). Meanwhile, the decreased absorbance of $-CO_3$ and −OH groups should be associated with the reaction of the precursor and glucose. After further silica coating, several broad absorptions assigned to −Si−O−Si− (1091 cm^{-1}) and Si−OH (950 cm^{-1}) show the generation of SiO_2 due to the hydrolysis of TEOS. Two typical sharp peaks of $-CH_3$ (2924 cm^{-1}) and $-CH_2$ (2853 cm^{-1}) are ascribed to the introduced CTAB. After calculation, the peaks of SiO_2 are kept and the peak of GdOF (485 cm^{-1}) appear (Supporting Information Figure S4d).

In the N_2 adsorption/desorption isotherm of GdOF:Ln@SiO_2 (Supporting Information Figure S5a), a typical IV-type isotherm with H1 hysteresis loops is apparent, showing the mesoporous structure. The BET surface area, total pore volume, and the average pore width are calculated to be 329 m^2/g, 0.2994 cm^3/g, and 3.53 nm, respectively. The pore size distribution shows the main size focuses at 2.24 nm. However, another wide peak at 118.4−131.6 nm (Supporting Information Figure S5b) should be attributed to the large cavity caused by the burning of carbon layer. The presence of diverse pore structure is characteristic for the yolk-like structure with mesoporous shell.

Different codoped rare earth ions can generate different visible light, which can provide various choices of the donors to transfer needed energy to PDT and PTT agents. It is known that ZnPc PSs are sensitive to red emissions;[46] we therefore measured the UC emissions of GdOF:*x*%Yb/1%Er@SiO_2 with different Yb^{3+} concentration to obtained brighter red emission. In Figure 3a, three main emissions at 521, 540, and 655 nm correspond to $^2H_{11/2} \rightarrow {}^4I_{15/2}$, $^4S_{3/2} \rightarrow {}^4I_{15/2}$, and $^4F_{9/2} \rightarrow {}^4I_{15/2}$, respectively.[59−61] Additionally, a weak emission peak at 490 nm assigned to $^2H_{9/2} \rightarrow {}^4I_{15/2}$ can also be detected (left, Figure 3a). In general, the emission cannot be observed for the low efficiency of the three/four-photon UC process and strong scattering of the host lattices. This appearance proves that the resulting GdOF samples are good hosts and silica has no obvious side effect to UC efficiency. Through integration of the green (500−600 nm) and red (600−700 nm) regions, it can be seen that the red emission becomes higher while the integrated green spectra becomes lower (Figure 3b). The red/green emission ratio changes from the initial value of 0.25 to 1.90 when the Yb^{3+} concentration is altered from 0 to 15%. In Figure 3c, the total integration of the intensity indicates that the optimized concentration of is 10%. It is well accepted the higher amount of doped Yb^{3+} dopants will decrease $Yb^{3+} \rightarrow Er^{3+}$ interatomic distance and thus facilitate back-energy-transfer from Er^{3+} to Yb^{3+}, which will consequently suppress the population in excited levels of $^2H_{9/2}$, $^2H_{11/2}$, and $^4S_{3/2}$, resulting in the decreased UC emissions. Accordingly, the emission color changes from green (0−2%) to yellow-green (5−10%) and then to yellow (15%) (Figure 7d). The red and green emission intensity as a function of the laser pump power indicates that green and red emissions are both two-photon transfer processes. It should be noted that GdOF:10%Yb/1%Er has a similar green emission to that of as-proposed brightest $NaYF_4$:10%Yb/1%Er prepared at co-precipitation route (Supporting Information Figure S6),[55] while the red emission is obviously higher. This result suggests GdOF is an even more effective UCL host, especially for red emission.

It has been reported that suitable doping amount of Mn^{2+} can effectively enhance the red emission.[55] To achieve higher red emission, we prepared GdOF:10% Yb/1%Er/*x*%Mn@SiO_2 with altered Mn^{2+} doping and the UC emission spectra under 980 nm NIR excitation are given in Figure 4a. The corresponding integrated R/G ratio and the integrated intensity are displayed in Figure 4b. As shown, the red intensity increases obviously while the green emissions decrease slightly, and the R/G emission ratios enhanced from 1.92 to 3.42 when the Mn^{2+} concentration is raised from 0 to 6%. Meanwhile, the blue emissions almost do not change with the doped Mn^{2+} (below, Figure 4a). Such an R/G emission enhancement should arise from the changed surrounding environment of light-emitting of Er^{3+} ions and the cross-relaxation of energy between Er^{3+} and Mn^{2+} ions. In Figure 4c, GdOF:10%Yb/1%Er/4% Mn@SiO_2 dispersed in PBS still keeps high dispersion after 20 min standing, and the solution presents strong pure red emission under the 980 nm NIR irradiation. The brilliant red-light line further proves the high-dispersed character of the as-prepared microcapsules. In the energy transfer mechanism (Figure 4d), the $^2H_{11/2}$ and $^4S_{3/2}$ levels of Er^{3+} to the $^4T_1$ level of

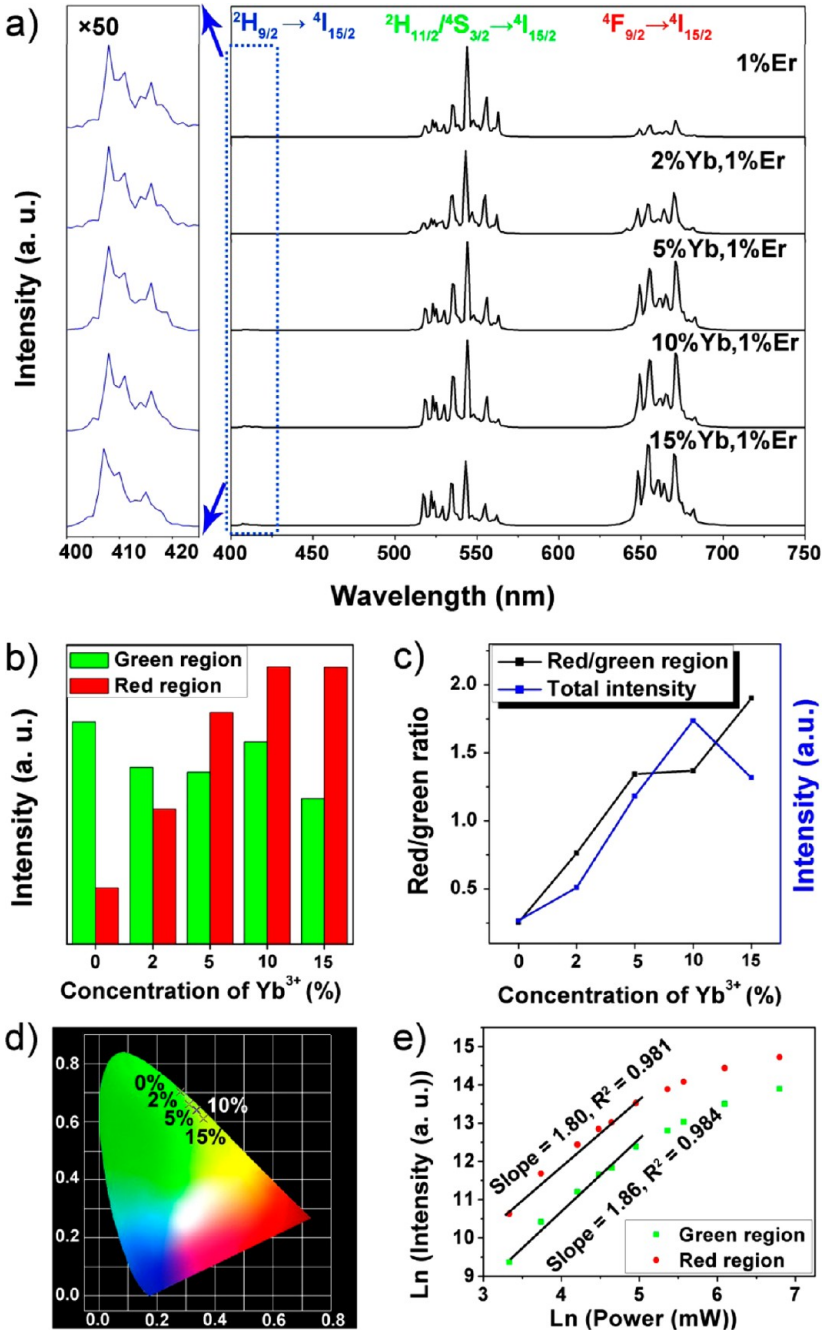

Figure 3. (a) UC emission spectra of GdOF:*x*%Yb/1%Er@SiO_2 (*x* = 0, 2, 5, 10, and 15) under 980 nm excitation. (b) Integrated intensity of red and green region. (c) Total integrated intensity and the red/green ratio with different concentration of Yb^{3+} ions. (d) CIE chromaticity diagram as a function of doped Yb^{3+} concentration. (e) Red and green emission intensity relationship with dependence of the laser pump power.

Mn^{2+} can contribute to the decreased green emission, and then the following back-energy transfer from the $^4T_1$ level of Mn^{2+} to the $^4F_{9/2}$ level of Er^{3+} can cause the enhanced red emission. To further prove the energy transfer from Er^{3+} to Mn^{2+}, the decay curves of GdOF:10%Yb/1%Er/*n*%Mn @SiO_2 (*n* = 0, 2, 4, and 6) at wavelength of 540 nm under the 980 nm excitation are depicted in Supporting Information Figure S7. With the increase of Mn^{2+} concentration, the lifetime of Er^{3+} ions decreases from 3.55 to 0.82 ms. The decreased emission efficiency is due to the photon-coupling of $^2H_{11/2}$ and $^4S_{3/2}$ levels of Er^{3+} ions and the $^4T_1$ level of Mn^{2+} ions, which decreases the radiative decay rates of Er^{3+} ions. Interestingly, when 2% Mn^{2+} ions was introduced, the lifetime decreases obviously than those of 2%−4% or 4%−6%. This result further proves the nonradiative transfer of Er^{3+} to Mn^{2+}.

Figure 5a shows the absorption spectrum of ZnPc solution (blue line). The ZnPc photosensitizers have an obvious absorption band at 650−680 nm. According to

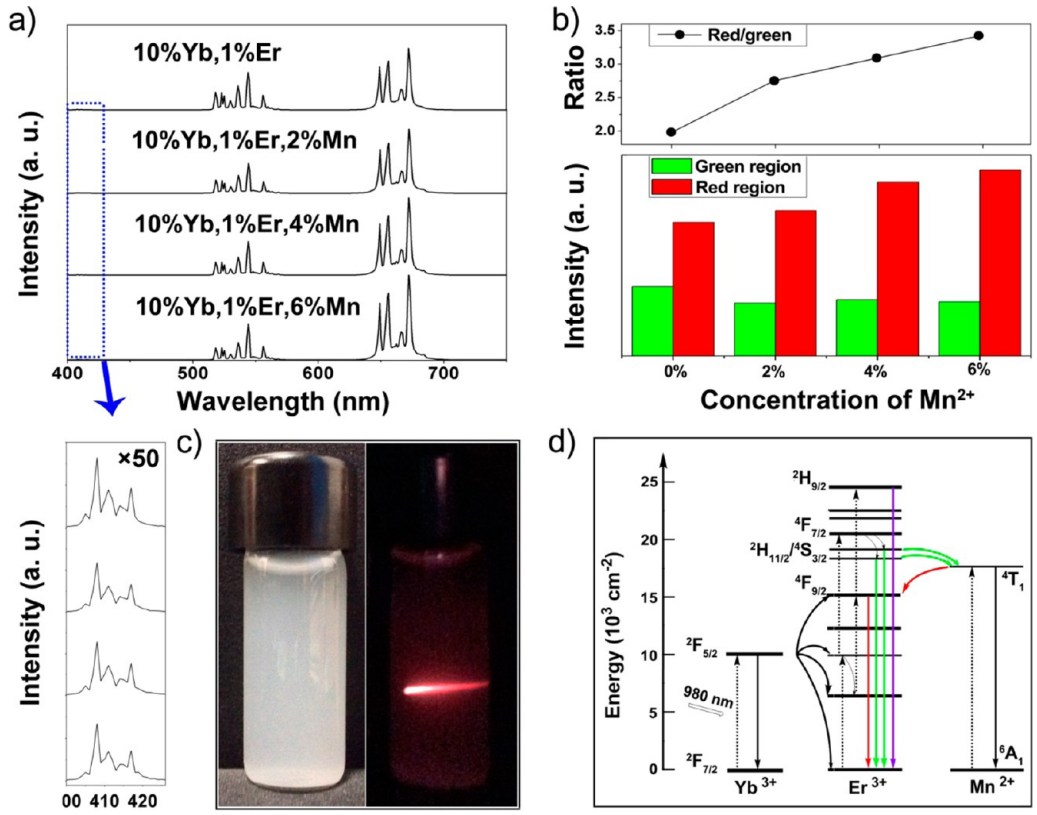

Figure 4. (a) UC emission spectra of GdOF:10%Yb/1%Er/*n*%Mn@mSiO$_2$ (*n* = 0, 2, 4, and 6) under 980 nm excitation. (b) (top) Red/green integrated intensity ratio and (bottom) integrated intensity of red and green region as a function of the doped Mn^{2+} concentration. (c) Luminescent photographs of GdOF:10%Yb/1%Er/4%Mn@*m*SiO$_2$ dispersed in the deionized water without and with NIR irradiation taken in a dark room. (d) Energy level diagram of the Yb^{3+}/Er^{3+}/Mn^{2+} doped UC mechanism.

the Förster theory, the red emission intensity of GdOF:10%Yb/1%Er/4%Mn@SiO_2 is much higher (3.08 times) than that of green region. Thus, there is a large overlap between the UC host and ZnPc PSs which can produce singlet oxygen effectively. After the conjunction of ZnPc, the red region emissions of GdOF:Ln@SiO_2 decrease obviously which is due to Förster resonance energy transfer from UCL host to ZnPc PSs.[46] Figure 5b presents the absorption spectra of UCMCs after added DPBF with and without NIR irradiation. It is apparent that the absorption peaks of the solution in the visible region decreases when irradiated by NIR light, which indicates singlet oxygen has been generated. Figure 5c shows the *in vivo* infrared thermal images of tumor-bearing mice after injection of 100 μL UCMCs (1 mg/mL) and saline as a function of the exposure time under NIR irradiation (0.6 W/cm^2), and the enhanced temperature curve *versus* the irradiation time (0−10 min) is displayed in Supporting Information Figure S8. The first group shows an obvious enhanced temperature from 36.0 to 50.9 °C, which can effectively kill the targeted tumor cells.[62] The absorption spectra of UCMCs with added DPBF *versus* irradiation time are also detected, as shown in Supporting Information Figure S9. The intensity decreases with prolonged time, indicating the singlet oxygen generates gradually. Thus, the as-prepared product should simultaneously have the photodynamic and photothermal effect.

Biocompatibility, *in Vitro* Drug Release and Cellular Cytotoxicity Assays under 980 nm NIR Irradiation. Cell viability of L929 fibroblast cells incubated for 24 h by UCMCs with varied concentrations is given in Figure 6a. The high cell viability (90.8−107.2%) in the whole range shows the good biocompatibility of UCMCs. Figure 6b presents the hemolysis result which guarantees the applicability *in vivo*. The red solutions inset are owing to the presence of hemoglobin. No visually red color is found with varied concentration from 15.63 to 500 μg/mL, suggesting negligible hemolysis with different solution added. The highest hemolytic efficiency of UCMCs is 0.17%, which is almost not hemolytic. It is thus inferred that the blood compatibility of UCMCs is excellent and it is almost nontoxic to live cells.

DOX was chosen as a typical anticancer drug to assay the carrying and release properties of UCMCs. The achieved high drug loading efficiency (92.8%) should be attributed to the large specific surface area and the electrostatic interaction between negatively charged mesoporous silica surface and positively charged DOX molecules. In addition, the pH-dependent drug-release behavior was detected. Usually, the pH value of normal cells in the human body is nearly

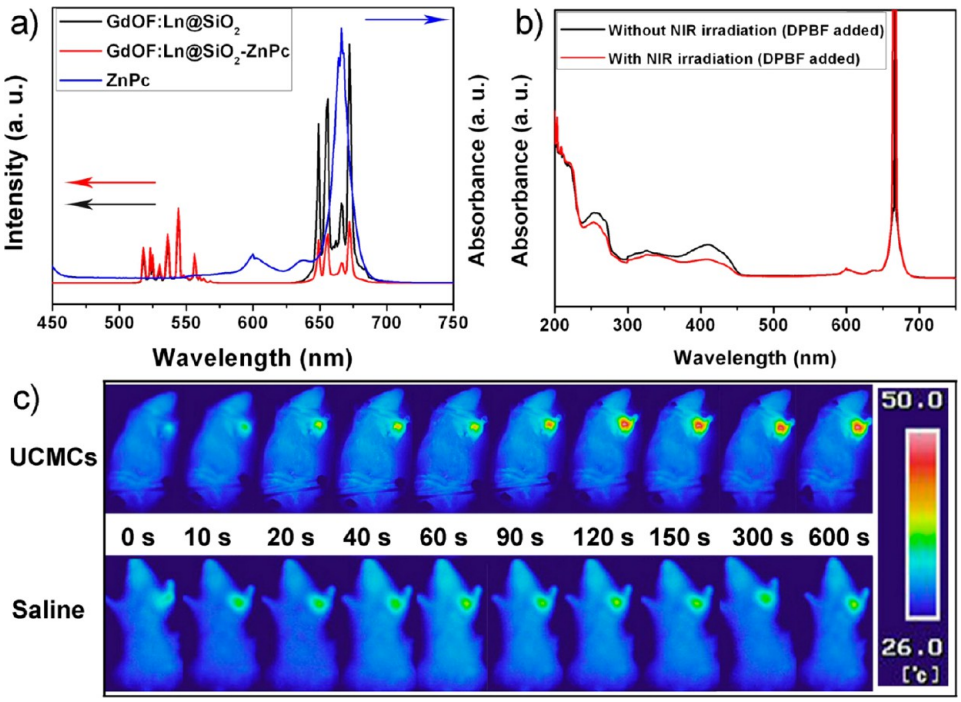

Figure 5. (a) Absorption spectrum of ZnPc (blue line), emission spectra of pure GdOF:Ln@SiO_2 (black line), and GdOF:Ln@SiO_2−ZnPc (red line) under 980 nm irradiation. (b) Absorption spectra of GdOF:Ln@SiO_2−ZnPc with added DPBF without and with NIR irradiation. (c) *In vivo* infrared thermal images of a tumor-bearing mouse after injection of GdOF:Ln@SiO_2−ZnPc-CDs as a function of the irradiation time under 980 nm NIR irradiation (0.6 W/cm^2).

neutral (pH = 7), while the pH value of cancer cells is lower owing to the excess metabolic product by the fast proliferation of cancer cells.[63] As shown in Figure 6c, only 35.7% of DOX has been released after 36 h (pH = 7). By comparison, for the release process with the pH value of 4, the carrier shows a faster and higher drug-release rate. During the beginning 1 h, 35.7% of DOX is released, and 77.5% of DOX has been released after 36 h. Moreover, when NIR irradiation is introduced, the release efficiency increases due to the thermal effect of UCMCs. The release efficiency is up to 91.6% under NIR irradiation at pH = 4, and the release efficiency is enhanced to 47.2% with irradiation under condition of pH = 7. During the antitumor therapy process, the initially rapid released DOX is essential to the therapy, which could effectively inhibit the growth of cancer cells. And the subsequent slow released DOX can continuously kill the cells survived from the initial stage. Meanwhile, we have also detected the release (leaching) of carbon dots from UCMCs, which shows a very low release rate due to the strong interaction between the amino groups on silica and carboxylated carbon dots (Supporting Information Figure S10).

It is well-known that the DOX has a wide absorbance peak in the visible region. Therefore, after loading DOX, the UCL intensity of UCMCs would reduce due to the quenching effect caused by the organic groups of DOX with high-frequency phonon vibrations.[64] The UC emission intensities of the samples with loaded DOX are detected with the released time. As shown in Figure 6d, the emissions could obviously be detected even with a high coverage of DOX ascribed to the strong UC emission of the system. The integrated emission intensities of UCMCs-DOX as a function of the release time with NIR irradiation (pH = 4) are given in Figure 6e. With the released DOX, the intensity increases gradually, and the mice could emit bright red UC emission under NIR irradiation after injection of UCMCs-DOX (inset, Figure 6e). Interestingly, the curve of integrated emission intensities with release time is much similar to the release efficiency curve, which suggests the great possibility to be tracked or monitored of this functional carrier by the emission during the therapy process. This UCL imaging result provides a considerable factor for the real-time bioimaging.

Figure 6f displays *in vitro* HeLa cells viabilities incubated for 24 h with free UCMCs, pure DOX, UCMCs-DOX with and without NIR irradiation with different concentrations. For HeLa cells incubated with pure UCMCs, the viability is 87.3−108.7%, indicating UCMCs are nontoxic to cancer cells. When pure DOX and UCMCs-DOX were added, the viability is reduced to 40.4−56.4% and 34.7−57.6%, respectively. It is interesting that UCMCs-DOX has higher inhibition than that of pure DOX under higher concentration, which is due to the better controlled release property for drug carrier. When UCMCs were added with NIR irradiation, the cell viability is 31.1−40.9%, revealing the photothermal and photodynamic effects caused by UCMCs under irradiation play a significant role in the

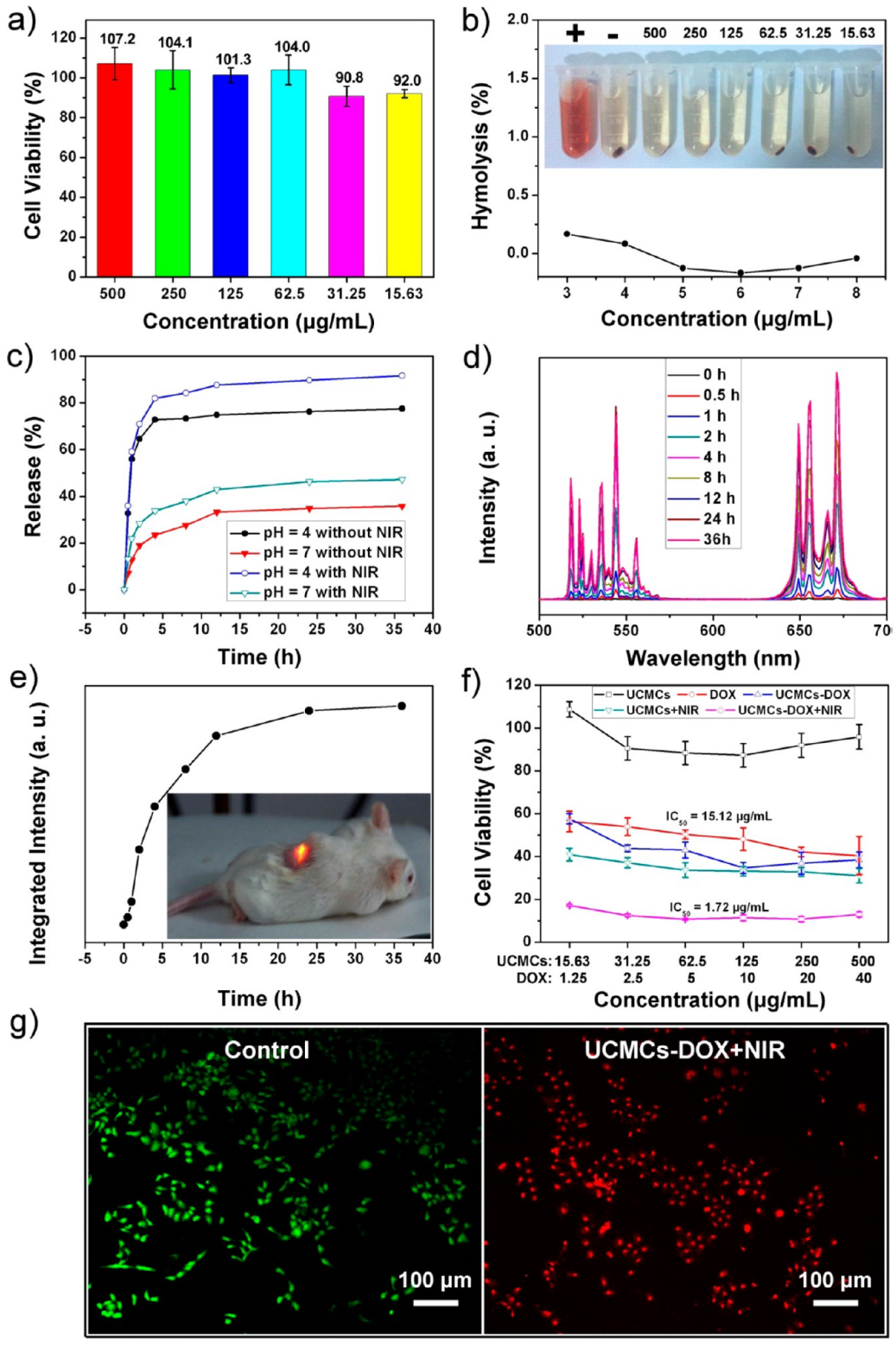

Figure 6. (a) The cell viability of L929 fibroblast incubated with UCMCs with different concentrations for 24 h. (b) Hemolytic percentage of UCMCs to human red blood cells. (c) DOX release efficiency of UCMCs-DOX at different pH values with and without NIR irradiation. (d) The emission intensity of UCMCs-DOX as a function of the release time (pH = 4 with irradiation). (e) The integrated intensity of the UC emission as a function of the release time; the inset is UC luminescence photograph under 980 nm irradiation. (f) *In vitro* viability of HeLa cells incubated for 24 h with DOX, UCMCs, UCMCs-DOX at different concentrations with and without NIR-laser irradiation. (g) Confocal laser scanning microscope (CLSM) images of HeLa cells incubated with culture without irradiation and incubated with UCMCs-DOX with NIR irradiation dyed with calcium AM and PI.

anticancer process. In particular, when UCMCs-DOX were added under irradiation by NIR laser, the cell viability is only 10.7−17.2%. The IC_{50} value of UCMCs-DOX under NIR irradiation is calculated to be

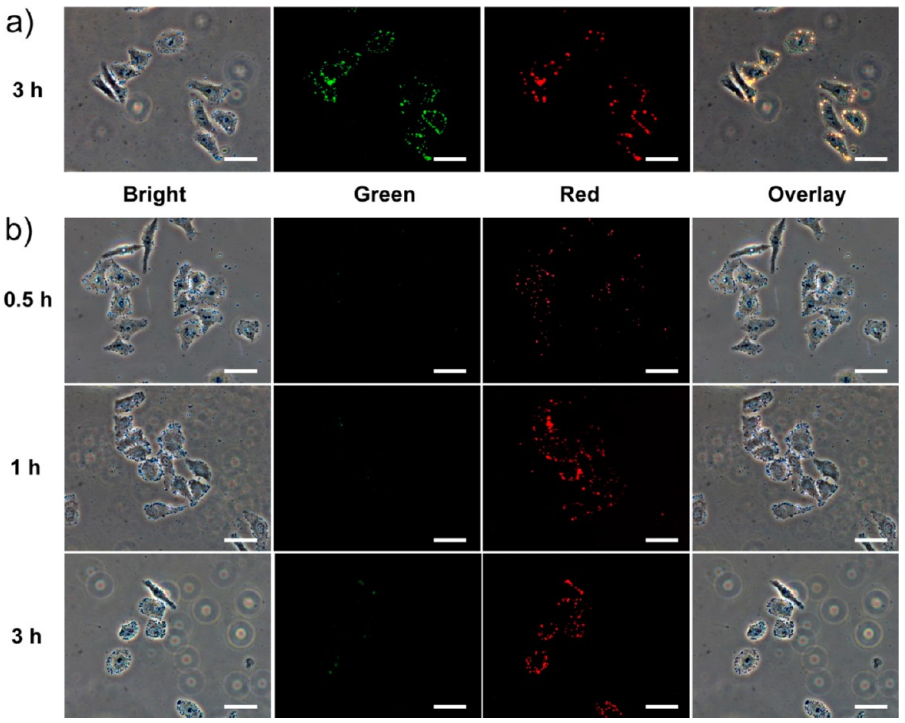

Figure 7. Inverted fluorescence microscope images of HeLa cells incubated (a) with UCMCs for 3 h and (b) with UCMCs-DOX for 0.5, 1, and 3 h at 37 °C. Scale bars for all the images are 50 μm.

1.72 μg/mL, which is markedly lower than that of pure DOX (15.12 μg/mL). The *in vitro* cytotoxicity indicates that an obvious synergistic effect of photothermal, photodynamic, and chemo-therapy stimulated NIR irradiation. Figure 6g shows the CLSM photographs of HeLa cancer cells incubated with culture only and with UCMCs-DOX under irradiation. Here, Calcein AM (which could mark living cells with green color) and propidium iodide (PI) (which could mark died cells with red color) were employed to dye the HeLa cells under different conditions, which were detected by CLSM to prove the killing effect. It is obvious that the cells are effectively killed incubated with UCMCs-DOX under NIR irradiation.

Supporting Information Figure S11 presents CLSM photographs of HeLa cancer cells incubated with UCMCs-DOX for 0.5, 1, 3, and 6 h in order to assay the cell uptake process. The blue fluorescence from the DAPI is used to mark the nuclei, and the red emission from UCMCs-DOX is employed to track the carrier. And the merged images of the two channels are also given correspondingly. In the first 0.5 h, there is little red emission, revealing only a few of UCMCs-DOX has been taken up by HeLa cells. Stronger red emission is observed in both the cytoplasm and the cell nucleus with prolonging time, suggesting that more particles are localized in the cells. The results suggest UCMCs can be effectively taken up by tumor cells as DOX loaded carrier.

To further study the uptake of UCMCs, we incubated another three groups of HeLa cells with pure culture, UCMCs-DOX, and pure UCMCs under the same condition for 3 h, respectively. After that, the cells were fixed by glutaraldehyde and dyed with DAPI, and then they were detected by CLSM. In Supporting Information Figure S12a1,a2 for the cells incubated with pure culture, no fluorescence can be detected under 552 nm excitation. When incubated with UCMCs-DOX, the cells show strong red emission deriving from DOX in the UCMCs-DOX composite (Supporting Information Figure S12b2). In Supporting Information Figure S12c2 for the cell incubated with pure UCMCs, the red emission can be clearly observed due to the down-conversion luminescence of doped Yb^{3+}/Er^{3+} when excited at 552 nm. The blue emission from DAPI is also clear in Supporting Information Figure S12c3. The three images (Supporting Information Figure S12c1−c3) reveal that the UCMCs can be successfully taken by the cells instead of merely attached on the cell boundary. It is thus inferred that the UCMCs-DOX can transfer into the cells instead of DOX itself.

UCL/CT/MRI Trimodal Imaging Properties of UCMCs. Figure 7 gives the respective inverted UC florescence microscope image of HeLa cells incubated with UCMCs and UCMCs-DOX, measured by a confocal microscope equipped with a 980 nm NIR laser. We can find that the UC luminescence of UCMCs emit bright yellow-red light (Figure 7a). UCMCs-DOX emits red light while green emission decreases (Figure 7b). The images with incubation time of 0.5, 1, and 3 h indicate the materials gradually enter the cells, which is consistent with above CLSM result. Meanwhile, the luminescence

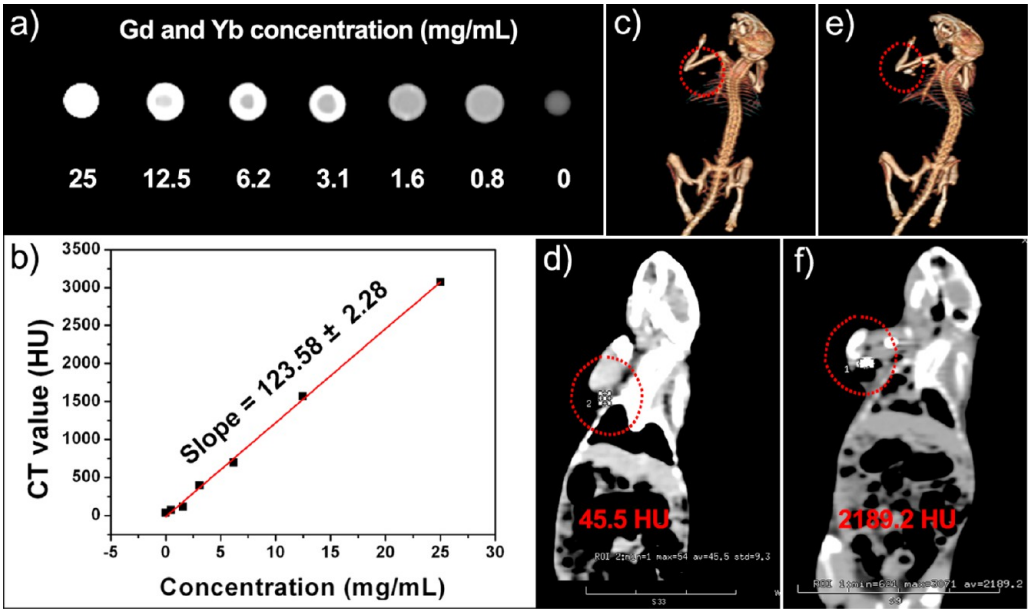

Figure 8. (a) *In vitro* CT images of UCMCs of different concentrations. (b) CT value of aqueous solution of UCMCs as a function of the concentration. CT imaging of tumor-bearing Balb/c mouse (c and d) before intratumor injection and (e and f) after injection.

enters the cells completely, which further proves that the product has been internalized into the cells rather than merely stained the surface of membrane. The results also suggest that the UCMCs and UCMCs-DOX are promising candidates for high-contrast *in vitro* bioimaging with low background.

Due to the deep tissue penetration and high resolution, X-ray CT has been proved an important diagnostic imaging technique. Gd/Yb doped particles can be used as contrast agents for CT imaging. Thus, we assessed CT contrast efficacy of UCMCs *in vitro* and *in vivo*, as shown in Figure 8a. The signal clearly increases with enhanced concentration of UCMCs. Compared with the literature, UCMCs show much higher positive contrast enhancement with high slope of 123.58.[40] *In vivo* CT imaging was further studied by intratumoral injection (Figure 8b–f) the CT value in the tumor is up to 2189.2 HU (Hounsfield units) compared with the control (without injection) of 45.5 HU from the transversal position. The results show the as-prepared UCMCs are effective contrast agent for CT imaging.

To study the potential application of UCMCs in MR imaging, we measured the dual mode (T_1 and T_2) contrast effects of UCMCs, as shown in Supporting Information Figure S13. The brighter signals in T_1-weighted images and the darker signals in T_2-weighted images are both detected with enhanced Gd concentration, demonstrating the simultaneous T_1- and T_2-weighted MRI effects. The respective longitudinal (r_1) and transverse (r_2) relaxivity value calculated from the curve fitting of relaxation time as a function of Gd concentration is 0.81 and 19.33 mM^{-1} s^{1-}. Interestingly, different from the reports of gadolinium-based materials as good T_1 contrast agents,[65,66] this composite works as an obviously better T_2 agent than the common Gd–DTPA complex, indicating that UCMCs could be used as a potential contrast agent for MR imaging.

***In Vivo* Synergistic Therapy under 980 nm Laser Irradiation.** The good biocompatibility and synergistic anticancer effect *in vitro* stimulates us to study the effect *in vivo*. Here, H22 tumor-bearing mice were injected intratumorally with UCMCs-DOX treated by different methods. The mice were studied when the tumor size grew to 6–10 mm in size (1 week). After various treatments of five groups, the result of each group is given in Figure 9a. It is obvious that the tumor size is very large without any injection. When pure DOX and UCMCs-DOX were injected, the tumors are inhibited to some extent. When NIR irradiation is utilized, remarkable inhibition occurs derived from the simultaneous PTT, PDT and enhanced chemotherapy. The marked difference indicates that the NIR irradiation plays a fundamental role in the therapy result. From Figure 9b,c, we can see the tumor sizes of the control group boomingly increase, while the sizes of the group injected UCMCs-DOX under NIR irradiation showing best results of the treatment almost stop to increase and even decrease. The body weight of different groups with enhanced time indicates the tumor weight is a considerable part of the body mass (Figure 9d). Figure 9e presents the tumor histologic section of the control group and the best treated group. By comparison, for the best inhibition group, the number of apoptotic and necrotic tumor cells has been markedly increased compared with control group.

Figure 10 shows H&E stained images of the heart, lung, kidney, liver, and spleen organs from different

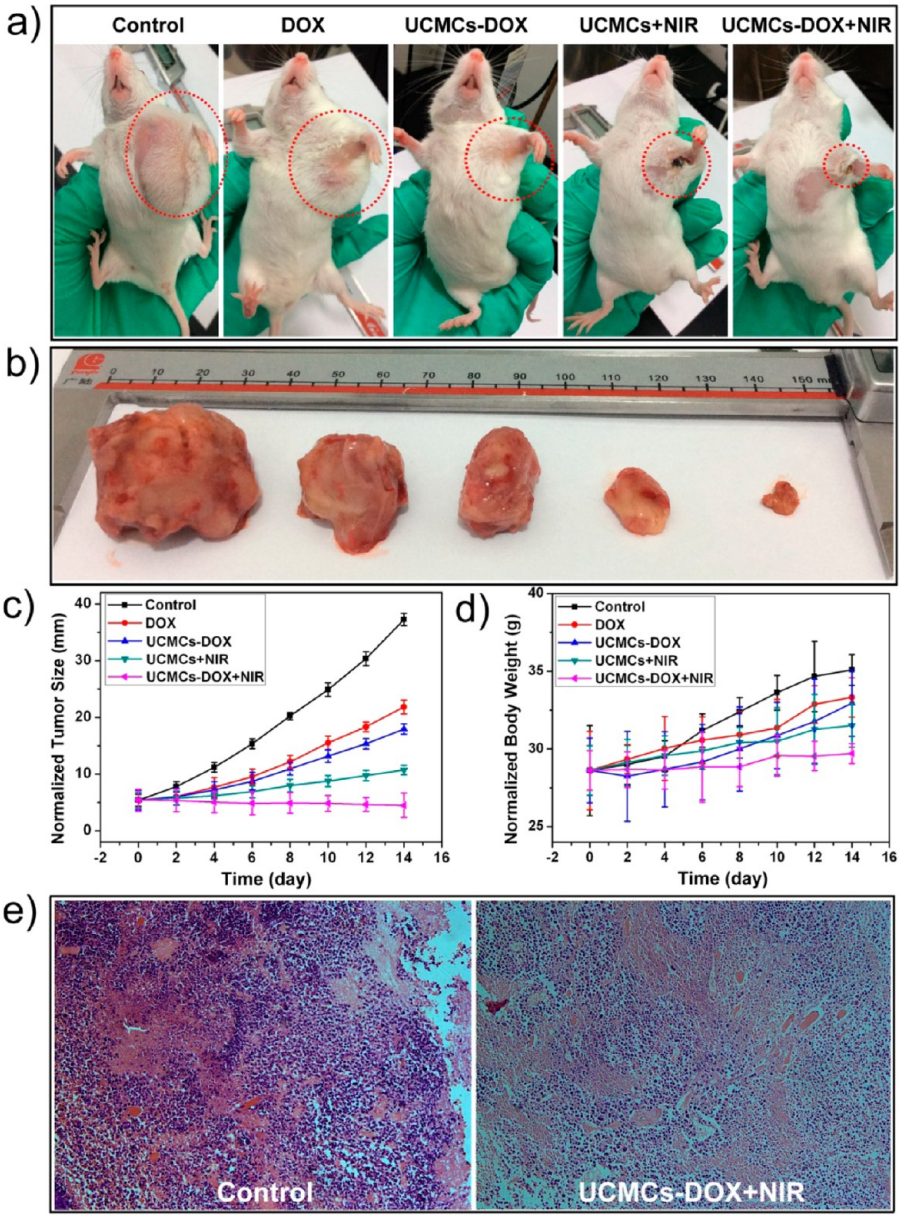

Figure 9. (a) Representative photographs of mice after various intratumoral treatments: without anything, pure DOX, UCMCs-DOX, UCMCs under NIR irradiation, and UCMCs-DOX under NIR irradiation. (b) Photographs of tumor tissue obtained after 14 days. (c) The tumor size and (d) body weight of H22 tumor in different groups after treatment. (e) H&E stained images of tumors from the controlled group and the best treated group.

groups. For the control group, the intercellular gap is ambiguous in the liver organ and there is remarkable atrophy in the glomerulus. There is slight inflammation in the pure DOX and UCMCs-DOX treated group. Meanwhile, the glomerulus in the groups of DOX, UCMCs-DOX treated group shows a slight atrophy phenomenon. The phenomenon does not decrease with the decrease of tumor sizes. In addition, compared with the control group, the organs taken from the group with the best results of the treatment (UCMCs-DOX+NIR) show the following results: Hepatocytes in the liver samples are found normal. No pulmonary fibrosis is detected in all the lung samples, and the glomerulus structure in the kidney section is observed clearly. The results clearly demonstrate the potential clinical applicability of UCMCs as antitumor carriers.

When referred to the clinical application, the intravenous administration of the as-prepared materials is necessary. First, GdOF:Ln@SiO_2−ZnPc-CDs-FA is preferentially internalized *via* a receptor-mediated endocytosis process, which is proved by the CLSM images in Supporting Information Figure S14. Supporting Information Figure S15a shows the infrared thermal images of a tumor-bearing mouse after intravenous injection of saline and UCMCs as a function of irradiation time, and the corresponding temperature curves are displayed in Supporting Information Figure S15b. The first group shows an obvious

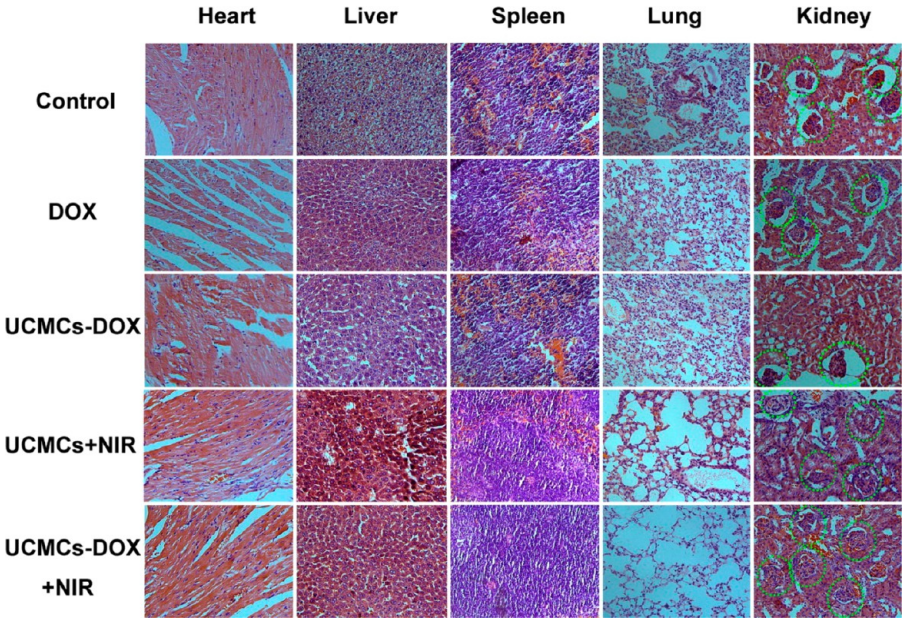

Figure 10. H&E stained images with different magnification of heart, liver, spleen, lung, and kidney from different groups.

enhanced temperature from 36.0 to 49.7 °C, which is near to the highest temperature (50.9 °C) with the intratumoral injection. The result indicates that the intravenously injected UCMCs could be recognized and targeted to the tumor cells due to the receptor-mediated endocytosis.

When the tumors grew to 8−12 mm in size, the mice were separated to five groups randomly for intravenous injection: the control group without any treatment, the pure DOX group, the UCMCs-DOX group, the UCMCs group under NIR irradiation, and UCMCs-DOX group under NIR irradiation. As shown in Supporting Information Figure S16a, the five groups almost present the same tendency compared with intratumoral administration because the FA-conjugated UCMCs can be targeted to the tumor cells which can effectively kill the tumor cells. Interestingly, there is a higher inhibition in the UCMCs-DOX group than that in the pure DOX group because more DOX can be transported into the cells based on the intracytoplasmic delivery of UCMCs compared to the passive diffusion of free DOX. Meanwhile, for the fifth group with injection of UCMCs-DOX under NIR irradiation, the tumor is almost completely inhibited and the size is similar to the initial dimension due to the synergistic (photothermal/photodynamic/chemo-) therapy effect (Supporting Information Figure S16b). In addition, Supporting Information Figure S16c shows that the body weights of all the groups increase with prolonged time, suggesting UCMCs may have no side effect to the mice. The cross-reference of the therapeutic effect with intravenous and intratumoral administrations to tumor cells is shown in Supporting Information Figure S17. The tumor images of the two groups injected with UCMCs-DOX under NIR irradiation are presented in Supporting Information Figure S17a. There is no obvious difference for the normalized tumor sizes between the two groups (9.43 mm and 8.23 mm), and the P value is 0.1407 (no significant difference) (Supporting Information Figure S17b).

The biodistribution and blood circulation of UCMCs with different intravenous injection times were detected by ICP-OES to evaluate the potential toxicity. Meanwhile, the two main metabolism methods of urine and feces were collected to detect the elimination. As shown in Figure 11a, in the early stages (30 min, 1 h, 4 h, 12 h, and 24 h after the injection), the particles accumulate in the livers, spleens, and lungs. In the whole detection times, the Gd concentration keeps low in heart and kidney. After 24 h of injection, the Gd concentration reduces in all the organs. In the 7th and 14th day after injection, the particles in the liver, spleen, and lung are much less than the first day. The results reveal that the injected UCMCs could be excreted from the mice with prolonged times. Figure 11b shows the pharmacokinetics of blood circulation curve. The fitted curve presents a two-compartment model with the first and second phase blood circulation half-lives at 0.336 ± 0.168 and 22.4 ± 5.21 h, respectively. The longer circulation of UCMCs is beneficial to biomedical diagnosis and therapy as drug carrier, including hepatic metastases and angiography. The metabolism of the UCMCs (1, 3, 7, and 14 day) is displayed in inset of Figure 11b. The Gd concentration in the urine keeps low in all times, indicating the kidney may be not the main metabolism organ for the particles. This result combined with the biodistribution result of the kidney could be strong evidence to prove that Gd^{3+} ions cannot release from UCMCs. In the feces collected from the first day, 61.3% of UCMCs has been

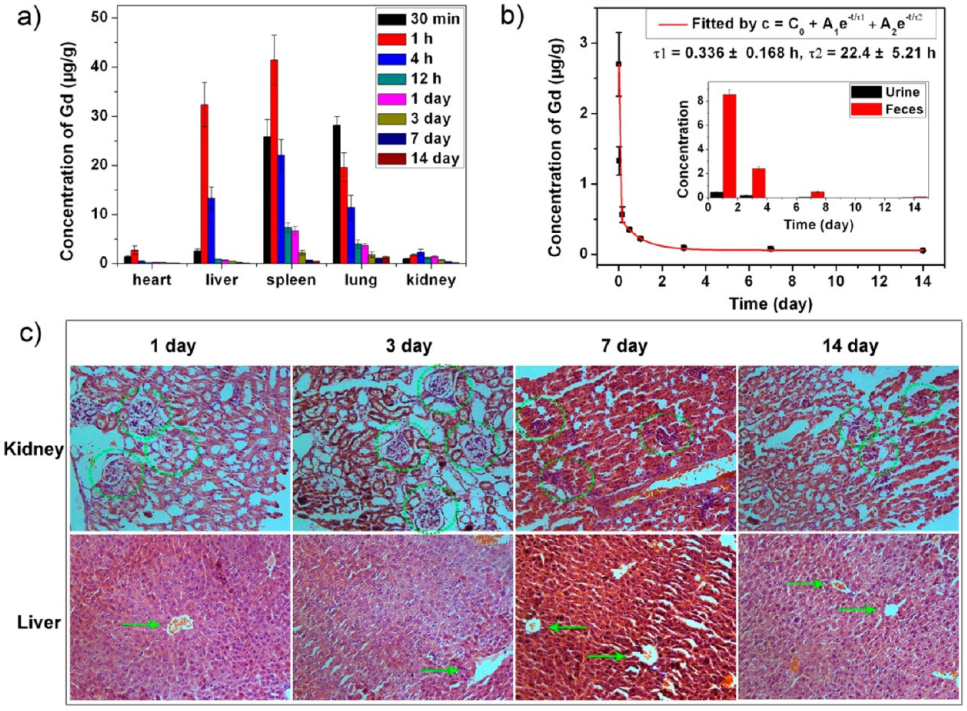

Figure 11. (a) The biodistribution in the main organs and (b) blood circulation in H22 mice after intravenous injection of UCMCs. Inset is the metabolism concentration with different times. (c) The corresponding H&E images of the kidneys and livers of the mice.

eliminated by the liver through the bile. The reason for this result may be due to the larger size of the as-synthesized UCMCs which have lower kidney toxicity. The H&E images of the livers and kidneys with different times (Figure 11c) indicate that UCMCs have no obvious side effect to the livers and kidneys. In conclusion, the UCMCs administrated with intravenous injection also present a high synergistic antitumor effect with low toxicity to the mice, which has a potential application in the clinical antitumor therapy.

CONCLUSIONS

In summary, GdOF:Ln@SiO_2—ZnPc-DCs yolk-like mesoporous microcapsules using effective UCL GdOF:Ln as cores and mesoporous silica layer as shell with hollow cavities have been fabricated by a unique route and applied for both multiple imaging (CT, MRI, UCL, photothermal) and multiple therapies (PDT, PTT, and chemotherapy). Due to the codoped Yb/Er/Mn, the enhanced red emission transfers energy to ZnPc PSs, which provide a high $^1O_2$ production, and the decorated carbon dots (CDs) generate an obvious thermal effect after NIR irradiation. The as-prepared product shows large surface area, good biocompatibility and high ablation efficiency to cancer cells owing to the synergistic therapeutic effect arising from PTT assigned to carbon dots, PDT ascribed to ZnPc PSs, and enhanced thermo-therapy from DOX, which are simultaneously triggered by a single 980 nm NIR laser irradiation. The animal experiment and histologic section analysis indicate the cancer can be markedly inhibited with organs undamaged. All the results indicate the multifunctional product should be very promising in cancer diagnose and therapy due to the effective multiple imaging and multimodal therapies.

EXPERIMENTAL SECTION

Reagents and Materials. All the chemical reagents are of analytical grade and used without any further purification, including nitric acid (HNO_3), urea, ammonium hydroxide ($NH_3 \cdot H_2O$), potassium fluoride (KF), cetyltrimethylammonium bromide (CTAB), tetraethyl orthosilicate (TEOS) (from Beijing Chemical Corporation, Beijing, China), Gd_2O_3, Yb_2O_3, Er_2O_3, Ho_2O_3, and Tm_2O_3 (99.99%) (from Sinopharm Chemical Reagent Co., Ltd., Beijing, China), phosphate buffered saline (PBS), potassium hydrogen phthalate (PHP), (Tianjin Kermel Chemical Reagent Co., Ltd., Tianjin, China), 3-aminopropyltrimethoxysilane (APTS), folic acid (FA), 1-(3-dimethy laminopropyl)-3-ethylcarbodiimide hydrochloride (EDC), doxorubicin (DOX), *N*-hydroxysuccinimide (NHS), 3-[4,5-dimethylthiazol-2-yl]-2,5-diphenyl tetrazolium bromide (MTT), 4′,6-diamidino-2-phenylindole (DAPI), dimethyl sulfoxide (DMSO), calcein AM, propidium iodide (PI), zinc(II)-phthalocyanine (ZnPc), 1,3-diphenylisobenzofuran (DPBF) (from sigma-Aldrich Co. LLC., Beijing, China).

Synthesis of $Gd(OH)_x(CO_3)_yF_2$:Ln Precursor. The well dispersed precursors were prepared *via* a precipitation process. $Ln(NO_3)_3$ were first prepared with Ln_2O_3 dissolved by HNO_3. Typically, 1 mol/L $Gd(NO_3)_3$ were prepared by dissolving corresponding Gd_2O_3 (18.1249 g) into HNO_3 (65%, 14.4 mol/L) with gradual heating and then diluted with deionized water to 100 mL. In a typical process, 1 mL of 1 M $Ln(NO_3)_3$, 0.1 mmol of KF, and 3 g of

urea were dissolved in 50 mL deionized water. After continuously stirring for 5 min, the mixture was heated to 90 °C and kept for 3 h. The resulting product was collected by centrifugation, which was repeated three times.

Synthesis of $Gd(OH)_x(CO_3)_yF_z$:Ln@C. Typically, 1.6 g of glucose was dissolved in a mixture of 18 mL of deionized water and 12 mL of ethanol. Then the as-prepared $Gd(OH)_x(CO_3)_yF_z$:Ln was added into the solution, the resulting suspension was transferred to a 50 mL autoclave and heated at 190 °C for 4 h. After that, the sample was rinsed with deionized water and ethanol several times.

Synthesis of GdOF:Ln@SiO_2 Capsules. Silica coating process was applied *via* a modified Stöber method.[67] Briefly, 0.2 g of as-prepared $Gd(OH)_x(CO_3)_yF_z$:Ln@C was ultrasonically dispersed in a mixed solution containing 50 mL of ethanol and 70 mL of deionized water. Subsequently, 0.3 g of CTAB, 0.3 mL of TEOS, and 1 mL of concentrated ammonium hydroxide were added to the mixed solution. After it was stirrED for 6 h, the as-obtained product was washed with deionized water and ethanol several times and dried in air at 60 °C for 12 h. Finally, the product was calcined in air at 700 °C for 3 h, and then GdOF:Ln@SiO_2 yolk-like capsules were obtained.

Covalent Conjunction of GdOF:Ln@SiO_2 with ZnPc Photosensitizers. The as-prepared GdOF:Ln@SiO_2 was first dispersed in 60 mL of deionized water. Subsequently, 0.15 mL of APTS was added to the solution and heated at 45 °C for 8 h with stirring, and then the sample was recovered by centrifugation, washed with ethanol and dried at 60 °C. The hydrophobic ZnPc were first dissolved in DMSO with concentration of 2 mg/mL. Then, 1 mL of ZnPc solution was added to the amino conjunct samples to obtain GdOF:Ln@SiO_2−ZnPc.

Modifying GdOF:Ln@SiO_2−ZnPc with Carbon Dots (CDs). The process was carried out by the literature with some modification.[68] First, 50 mg multiwall carbon nanotubes were added into 50 mL of mixed solution of HNO_3/H_2SO_4 (1:3 by volume), treated for 24 h at 80 °C with water reflux in order to cut nanotubes to nanodots. The as-prepared CDs solution was diluted to 1:10 and neutralized by NaOH for further use. Five milliliters of the neutral CDs solution was added to GdOF:Ln@SiO_2−ZnPc solution and the solution stirred for 2 h. The obtained product was denoted as GdOF:Ln@SiO_2−ZnPc-CDs.

Surface Modification of GdOF:Ln@SiO_2−ZnPc-CDs with FA. FA is conjugated onto the surface of GdOF:Ln@SiO_2−ZnPc-CDs by coupling effect of NHS and EDC. Typically, 1 mg of FA, 6 mg of EDC, and 2 mg of NHS were added into 20 mL of deionized water and the solution stirred for 2 h in dark. Then, 20 mg of GdOF:Ln@SiO_2−ZnPc-CDs capsules was added and the mixture stirred for one night in the dark. The product was recovered by centrifugation and washed with ethanol and deionized water to remove the free FA. The as-prepared product was denoted as GdOF:Ln@SiO_2−ZnPc-CDs-FA up-conversion microcapsules (UCMCs) for subsequent biological test.

Characterization. Powder X-ray diffraction (XRD) measurements were performed on a Rigaku D/max TTR-III diffractometer at a scanning rate of 15°/min in the 2θ range of 20−80°, using Cu Kα radiation (λ = 0.15405 nm). The morphology and structure were recorded on scanning electron microscope (SEM, JSM-6480A), transmission electron microscopy (TEM, FEI Tecnai G^2 S-Twin) and high-resolution transmission electron microscopy (HRTEM). Fourier transform infrared spectroscopy (FT-IR) spectra were obtained on a PerkinElmer 580B IR spectrophotometer using the KBr pellet technique. N_2 adsorption/desorption isotherms were recorded on a Micromeritics ASAP Tristar II 3020 instrument. Pore size distribution was determined by the Barrete-Jonere-Halenda (BJH) method. UC emission spectra were measured on a R955 (HAMAMATSU) from 400 to 800 nm using 980 nm laser diode module (K98D08M-30W, China) as the irradiation source. DOX concentration was detected by UV-1601 spectrophotometer. Inductively coupled plasma (ICP) was carried out on a Thermo Electron X Series II ICP apparatus. Dynamic lighting scattering (DLS) measurement was performed on a Malvern Zetasizer 1000HSA instrument.

Singlet Oxygen Detection of UCMCs. DPBF was employed to confirm singlet oxygen by measuring its absorption *via* UV−vis spectroscopy as a chemical probe.[69,70] In a typical procedure, 2 mL of ethanol solution of DPBF (10 mmol/L) was added to 2 mL of UCMCs solution and the mixture was transferred into a 10 mL cuvette. The solution was kept in the dark and irradiated by a 980 nm NIR laser for 5 min. Then, the solution was centrifuged and the supernatant was collected for UV−vis detection. For the control experiments, DPBF solution mixed with UCMCs without NIR laser irradiation was also measured for comparison under the same conditions.

***In Vitro* Cytotoxicity of UCMCs.** MTT was employed to evaluate the cytotoxicity of the products against HeLa cells. Briefly, HeLa tumor cells were seeded in a 96-well plate with the number of 8000 per well, then cultured at 37 °C for 12 h in 5% CO_2. After that, UCMCs, pure DOX, and UCMCs-DOX were introduced and incubated with cells at 37 °C for another 24 h in 5% CO_2. Among them, UCMCs and UCMCs-DOX incubated with HeLa cells with and without NIR irradiation were used to study the photo guided cytotoxicity effect. The samples were diluted into respective concentration of 15.63, 31.25, 62.5, 125, 250, and 500 μg/mL for MTT assay. Then, 20 μL of the MTT solution was added to each well. The plate was subsequently incubated for another 4 h at 37 °C. Finally, 150 μL of DMSO was added to each well and the samples were shaken for 10 min in order to completely blend solvent and the formazan. The absorbance was measured at 490 nm using a microplate reader. Optical density which received no drug was regarded as 100% growth. The *in vitro* viability of UCMCs was detected similar to the cytotoxicity MTT assay by incubation of L929 fibroblast cells instead of HeLa cells.

Hemolysis Assay of UCMCs. Red blood cells were obtained by removing the serum from human blood after washing with 0.9% saline, and centrifugated five times. After that, blood cells were diluted to 1:10 with PBS solution. Then, 0.4 mL of diluted cells suspension was mixed with 1.6 mL of PBS (as a negative control), 1.6 mL of deionized water (as a positive control), and 1.6 mL of product suspensions with varying concentration of 15.63, 31.25, 62.5, 125, 250, and 500 μg/mL. The eight samples were shaken and kept steady for 2 h. Finally, the mixtures were centrifuged and the absorbance of the upper supernatants was measured by UV−vis spectroscopy. The hemolysis percentage was calculated by the following equation: Hemolysis (%) = $(A_{sample} - A_{control(-)})/(A_{control(+)} - A_{control(-)})$, where A is the absorbance.

DOX Loading and Release Test. Typically, 30 mg of UCMCs was added into 5 mL of PBS and ultrasonically dispersed. Then, DOX (2.5 mg) was added into the solution and the mixture slowly stirred for 24 h. The solution was then centrifuged at 6000 rpm for 4 min, and the supernatant was recovered for UV−vis measurement. Ten milliliters of fresh PBS was replenished and placed in water bath kettle at 37 °C with stirring for 0.5 h; the supernatant solution was centrifuged and saved. The process was repeated at release time of 0.5, 1, 2, 4, 8, 12, 24, and 36 h, respectively. PBS solutions with the pH value of 4 and 7 were directly prepared by pH modifier. The loading capacity and release efficiency were determined by UV−vis spectra at the wavelength of 480 nm.

Cellular Uptake of UCMCs. Confocal laser scanning microscope (CLSM) was used to study the cellular uptake by HeLa tumor cells. Typically, HeLa cancer cells were cultured in a 6-well plate and grew overnight to get a monolayer. Then, the cells were incubated with as-prepared UCMCs-DOX at 37 °C for 0.5, 1, 3, and 6 h, respectively. After that, the cells were washed with PBS solution three times, fixed for 10 min with 2.5% formaldehyde (1 mL/well), and then rinsed with PBS several times. Subsequently, the nuclei were stained with DAPI solution (20 μg mL^{-1} in PBS, 1 mL $well^{-1}$) for 10 min in order to perform nucleus labeling. At last, the cells were rinsed with PBS three times. The coverslips were placed on a glass microscope slide, and the fluorescence imaging of the samples were recorded by CLSM apparatus (Leica TCS SP8).

UC Luminescence Microscopy (UCLM). For UC luminescence imaging, HeLa tumor cells were first seeded in 6-well culture plates and incubated for 12 h. Then the cells were incubated at 37 °C for 0.5, 1, and 3 h with UCMCs and UCMCs-DOX. The cells were further washed with PBS three times, fixed by 1 mL of formaldehyde (2.5%) in each PBS three times to detach the attached

nanoparticles. The UC imaging of the samples were recorded on Nikon Ti−S with an external 980 nm diode laser irradiation.

***In Vivo* Toxicity of UCMCs-DOX.** Female Balb/c (25−35 g) were purchased from Harbin Veterinary Research Institute, Chinese Academy of Agricultural Sciences (Harbin, China), and all the mouse experiments were performed in compliance with the criterions of The National Regulation of China for Care and Use of Laboratory Animals. First, the tumors were found by subcutaneous injection of H22 cells (murine hepatocarcinoma cell lines) in the left axilla of each female Balb/c mouse (20−25 g). After grown for 1 week, the tumors sizes reached about 6−10 mm with the body weight of 25−30 g. The tumor-bearing mice were randomized into five groups (n = 5, each group) and were treated by intratumoral injection with UCMCs, pure DOX, UCMCs-DOX, and UCMCs-DOX with NIR irradiation. The first group was used as blank control. The injected amount was 100 μL (1 mg/mL) every 2 days, and the pure DOX was consistent with UCMCs-DOX. For the NIR irradiation process, the tumor site was irradiated with 980 nm laser for 10 min after injecting different samples for 1 h. The body weights and tumor sizes were recorded every 2 days after the treatment.

***In Vitro* and *in Vivo* X-ray CT Imaging.** The *in vitro* CT imaging experiments were performed on a Philips 64-slice CT scanner at voltage of 120 kV. UCMCs-DOX were first dispersed in PBS with various concentrations of 25, 12.5, 6.3, 3.1, 1.6, and 0.8 mg/mL and then placed in a series of 2 mL tubes for CT imaging. To perform *in vivo* CT imaging, the Balb/c mice were first anesthetized with 10% chloral hydrate by intraperitoneal injection. Subsequently, 100 μL of UCMCs-DOX (50 mg/mL) was intratumorally injected into the tumor-bearing mouse *in situ*. The mouse was scanned before and after injection of the sample.

***In Vitro* and *in Vivo* T_1-Weighted MR Imaging.** The *in vitro* MR imaging experiments were carried out on a 0.5 T MRI magnet (Shanghai Niumai Corporation Ration NM120-Analyst). UCMCs-DOX were dispersed in water at various Gd concentrations. T_1 and T_2 measurements were performed using a nonlinear fit to changes in the mean signal intensity within each well as a function of repetition time (TR) with a Huantong 1.5 T MR scanner. Finally, the r_1 (r_2) relaxivity values were determined through the curve fitting of $1/T_1$ ($1/T_2$) relaxation time (s^{-1}) *versus* Gd concentration (mM).

Histology Examination. Histology analysis was carried out at the 14th day after treatment. The typical liver, kidney, and tumor tissues of the mice in the control group and treatment group were isolated. After that, the organs were dehydrated by buffered formalin, ethanol with different concentrations, and xylene, then embedded in liquid paraffin. The sliced organs and tumor tissues (3−5 mm) were stained with hematoxylin and eosin (H&E) and examined by CLSM (Leica TCS SP8).

Biodistribution, Circulation, and Metabolism. Balb/c mice were injected intravenously with UCMCs (dose = 20 mg/kg). The mice (n = 3) were euthanized at different time points (30 min, 1 h, 4 h, 12 h, 1 day, 3 days, 7 days, and 14 days). The two metabolism methods were detected by urine and feces which were collected in 1 day (0−24 h after injection), 3 days, 7 days, and 14 days. The blood and major organs (heart, liver, spleen, lung, and kidney) were collected and dissolved with 5 mL of HNO_3 and HCl (v/v = 1:3), and then heated at 70 °C for 5 min to obtain clear solutions. After that, the solutions were centrifuged and the supernatant was kept for further ICP-OES analysis.

Conflict of Interest: The authors declare no competing financial interest.

Supporting Information Available: XRD patterns of the samples obtained at different synthetic step; TEM images and digital photographs of carbon nanotubes and carboxylated carbon dots; DLS result of GdOF:Ln@SiO_2-ZnPc-CDs-FA UCMCs; FT-IR spectra; N_2 adsorption/desorption isotherm of GdOF:Ln@SiO_2 capsule. This material is available free of charge *via* the Internet at http://pubs.acs.org.

Acknowledgment. Financial support from the National Natural Science Foundation of China (NSFC 21271053, 21401032, 51472058, 51332008) and the National Basic Research Program of China (2014CB643803) are greatly acknowledged.

REFERENCES AND NOTES

1. Gai, S.; Li, C.; Yang, P.; Lin, J. Recent Progress in Rare Earth Micro/Nanocrystals: Soft Chemical Synthesis, Luminescent Properties, and Biomedical Applications. *Chem. Rev.* **2014**, *114*, 2343–2389.
2. Antaris, A. L.; Robinson, J. T.; Yaghi, O. K.; Hong, G.; Diao, S.; Luong, R.; Dai, H. Ultra-Low Doses of Chirality Sorted (6,5) Carbon Nanotubes for Simultaneous Tumor Imaging and Photothermal Therapy. *ACS Nano* **2013**, *7*, 3644–3652.
3. Jain, P. K.; Huang, X.; El-Sayed, I. H.; El-Sayed, M. A. Noble Metals on the Nanoscale: Optical and Photothermal Properties and Some Applications in Imaging, Sensing, Biology, and Medicine. *Acc. Chem. Res.* **2008**, *41*, 1578–1586.
4. Shi, J.; Wang, L.; Gao, J.; Liu, Y.; Zhang, J.; Ma, R.; Liu, R.; Zhang, Z. A Fullerene-Based Multi-Functional Nanoplatform for Cancer Theranostic Applications. *Biomaterials* **2014**, *35*, 5771–5784.
5. Zhen, Z.; Tang, W.; Chuang, Y.-J.; Todd, T.; Zhang, W.; Lin, X.; Niu, G.; Liu, G.; Wang, L.; Pan, Z.; *et al.* Tumor Vasculature Targeted Photodynamic Therapy for Enhanced Delivery of Nanoparticles. *ACS Nano* **2014**, *8*, 6004–6013.
6. Cao, B.; Yang, M.; Zhu, Y.; Qu, X.; Mao, C. Stem Cells Loaded With Nanoparticles as a Drug Carrier for *in Vivo* Breast Cancer Therapy. *Adv. Mater.* **2014**, *26*, 4627–4631.
7. Yuan, Y.; Liu, J.; Liu, B. Conjugated-Polyelectrolyte-Based Polyprodrug: Targeted and Image-Guided Photodynamic and Chemotherapy with On-Demand Drug Release upon Irradiation with a Single Light Source. *Angew. Chem., Int. Ed.* **2014**, *53*, 7163–7168.
8. Chatterjee, D. K.; Fong, L. S.; Zhang, Y. Nanoparticles in Photodynamic Therapy: An Emerging Paradigm. *Adv. Drug Delivery Rev.* **2008**, *60*, 1627–1637.
9. Kim, S.; Ohulchanskyy, T. Y.; Pudavar, H. E.; Pandey, R. K.; Prasad, P. N. Organically Modified Silica Nanoparticles Co-Encapsulating Photosensitizing Drug and Aggregation-Enhanced Two-Photon Absorbing Fluorescent Dye Aggregates for Two-Photon Photodynamic Therapy. *J. Am. Chem. Soc.* **2007**, *129*, 2669–2675.
10. Yang, P.; Gai, S.; Lin, J. Functionalized Mesoporous Silica Materials for Controlled Drug Delivery. *Chem. Soc. Rev.* **2012**, *41*, 3679–3698.
11. Liu, J.; Bu, J.; Bu, W.; Zhang, S.; Pan, L.; Fan, W.; Chen, F.; Zhou, L.; Peng, W.; Zhao, K.; *et al.* Real-Time *in Vivo* Quantitative Monitoring of Drug Release by Dual-Mode Magnetic Resonance and Upconverted Luminescence Imaging. *Angew. Chem., Int. Ed.* **2014**, *53*, 4551–4555.
12. Li, Y.; Shi, J. Hollow-Structured Mesoporous Materials: Chemical Synthesis, Functionalization and Applications. *Adv. Mater.* **2014**, *26*, 3176–205.
13. Zhang, S.; Ni, W.; Kou, X.; Yeung, M. H.; Sun, L.; Wang, J.; Yan, C. Formation of Gold and Silver Nanoparticle Arrays and Thin Shells On Mesostructured Silica Nanofibers. *Adv. Funct. Mater.* **2007**, *17*, 3258–3266.
14. Vallet-Regi, M.; Balas, F.; Arcos, D. Mesoporous Materials for Drug Delivery. *Angew. Chem., Int. Ed.* **2007**, *46*, 7548–7558.
15. Slowing, I. I.; Vivero-Escoto, J. L.; Wu, C. W.; Lin, V. S. Y. Mesoporous Silica Nanoparticles as Controlled Release Drug Delivery and Gene Transfection Carriers. *Adv. Drug Delivery Rev.* **2008**, *60*, 1278–1288.
16. Li, Z. X.; Barnes, J. C.; Bosoy, A.; Stoddart, J. F.; Zink, J. I. Mesoporous Silica Nanoparticles in Biomedical Applications. *Chem. Soc. Rev.* **2012**, *41*, 2590–2605.
17. Chen, Y.; Chen, H.; Guo, L.; He, Q.; Chen, F.; Zhou, J.; Feng, J.; Shi, J. Hollow/Rattle-Type Mesoporous Nanostructures by a Structural Difference-Based Selective Etching Strategy. *ACS Nano* **2010**, *4*, 529–539.
18. Sun, L.-D.; Wang, Y.-F.; Yan, C.-H. Paradigms and Challenges for Bioapplication of Rare Earth Upconversion Luminescent Nanoparticles: Small Size and Tunable Emission/Excitation Spectra. *Acc. Chem. Res.* **2014**, *47*, 1001–1009.
19. Moon, H. K.; Lee, S. H.; Choi, H. C. *In Vivo* Near-Infrared Mediated Tumor Destruction by Photothermal Effect of Carbon Nanotubes. *ACS Nano* **2009**, *3*, 3707–3713.

20. Chatterjee, D. K.; Gnanasammandhan, M. K.; Zhang, Y. Small Upconverting Fluorescent Nanoparticles for Biomedical Applications. *Small* **2010**, *6*, 2781–2795.
21. Gu, Z.; Yan, L.; Tian, G.; Li, S.; Chai, Z.; Zhao, Y. Recent Advances in Design and Fabrication of Upconversion Nanoparticles and their Safe Theranostic Applications. *Adv. Mater.* **2013**, *25*, 3758–3779.
22. Cheng, L.; Yang, K.; Li, Y.; Chen, J.; Wang, C.; Shao, M.; Lee, S.-T.; Liu, Z. Facile Preparation of Multifunctional Upconversion Nanoprobes for Multimodal Imaging and Dual-Targeted Photothermal Therapy. *Angew. Chem., Int. Ed.* **2011**, *50*, 7385–7390.
23. Xiao, Q.; Zheng, X.; Bu, W.; Ge, W.; Zhang, S.; Chen, F.; Xing, H.; Ren, Q.; Fan, W.; Zhao, K.; *et al.* A Core/Satellite Multifunctional Nanotheranostic for *in Vivo* Imaging and Tumor Eradication by Radiation/Photothermal Synergistic Therapy. *J. Am. Chem. Soc.* **2013**, *135*, 13041–13048.
24. Haase, M.; Schaefer, H. Upconverting Nanoparticles. *Angew. Chem., Int. Ed.* **2011**, *50*, 5808–5829.
25. Wang, F.; Banerjee, D.; Liu, Y.; Chen, X.; Liu, X. Upconversion Nanoparticles in Biological Labeling, Imaging, and Therapy. *Analyst* **2010**, *135*, 1839–1854.
26. Zhou, J.; Liu, Z.; Li, F. Upconversion Nanophosphors for Small-Animal Imaging. *Chem. Soc. Rev.* **2012**, *41*, 1323–1349.
27. Wang, L.; Dong, H.; Li, Y.; Xue, C.; Sun, L.-D.; Yan, C.-H.; Li, Q. Reversible Near-Infrared Light Directed Reflection in a Self-Organized Helical Superstructure Loaded with Upconversion Nanoparticles. *J. Am. Chem. Soc.* **2014**, *136*, 4480–4483.
28. Ehlert, O.; Thomann, R.; Darbandi, M.; Nann, T. A Four-Color Colloidal Multiplexing Nanoparticle System. *ACS Nano* **2008**, *2*, 120–124.
29. Ostrowski, A. D.; Chan, E. M.; Gargas, D. J.; Katz, E. M.; Han, G.; Schuck, P. J.; Milliron, D. J.; Cohen, B. E. Controlled Synthesis and Single-Particle Imaging of Bright, Sub-10 nm Lanthanide-Doped Upconverting Nanocrystals. *ACS Nano* **2012**, *6*, 2686–2692.
30. Zeng, S.; Wang, H.; Lu, W.; Yi, Z.; Rao, L.; Liu, H.; Hao, J. Dual-Modal Upconversion Fluorescent/X-Ray Imaging using Ligand-Free Hexagonal Phase $NaLuF_4$:Gd/Yb/Er Nanorods for Blood Vessel Visualization. *Biomaterials* **2014**, *35*, 2934–2941.
31. Abel, K. A.; Boyer, J.-C.; van Veggel, F. C. J. M. Hard Proof of the $NaYF_4$/$NaGdF_4$ Nanocrystal Core/Shell Structure. *J. Am. Chem. Soc.* **2009**, *131*, 14644–14645.
32. Sun, Y.; Zhu, X.; Peng, J.; Li, F. Core-Shell Lanthanide Upconversion Nanophosphors as Four-Modal Probes for Tumor Angiogenesis Imaging. *ACS Nano* **2013**, *7*, 11290–11300.
33. Chatterjee, D. K.; Rufaihah, A. J.; Zhang, Y. Upconversion Fluorescence Imaging of Cells and Small Animals using Lanthanide Doped Nanocrystals. *Biomaterials* **2008**, *29*, 937–943.
34. Feng, W.; Han, C.; Li, F. Upconversion-Nanophosphor-Based Functional Nanocomposites. *Adv. Mater.* **2013**, *25*, 5287–5303.
35. Meiser, F.; Cortez, C.; Caruso, F. Biofunctionalization of Fluorescent Rare-Earth-Doped Lanthanum Phosphate Colloidal Nanoparticles. *Angew. Chem., Int. Ed.* **2004**, *43*, 5954–5957.
36. Tu, D.; Liu, L.; Ju, Q.; Liu, Y.; Zhu, H.; Li, R.; Chen, X. Time-Resolved FRET Biosensor based on Amine-Functionalized Lanthanide-Doped $NaYF_4$ Nanocrystals. *Angew. Chem., Int. Ed.* **2011**, *50*, 6306–6310.
37. Yi, G.; Peng, Y.; Gao, Z. Strong Red-Emitting Near-Infrared-to-Visible Upconversion Fluorescent Nanoparticles. *Chem. Mater.* **2011**, *23*, 2729–2734.
38. Passuello, T.; Piccinelli, F.; Pedroni, M.; Polizzi, S.; Mangiarini, F.; Vetrone, F.; Bettinelli, M.; Speghini, A. NIR-to-Visible and NIR-to-NIR upconversion in Lanthanide Doped Nanocrystalline GdOF with Trigonal Structure. *Opt. Mater.* **2011**, *33*, 1500–1505.
39. Liu, F.; He, X.; Liu, L.; You, H.; Zhang, H.; Wang, Z. Conjugation of NaGdF4 Upconverting Nanoparticles on Silica Nanospheres as Contrast Agents for Multi-Modality Imaging. *Biomaterials* **2013**, *34*, 5218–5225.
40. Dai, Y.; Xiao, H.; Liu, J.; Yuan, Q.; Ma, P. A.; Yang, D.; Li, C.; Cheng, Z.; Hou, Z.; Yang, P.; *et al. In Vivo* Multimodality Imaging and Cancer Therapy by Near-Infrared Light-Triggered Trans-Platinum Pro-Drug-Conjugated Upconverison Nanoparticles. *J. Am. Chem. Soc.* **2013**, *135*, 18920–18929.
41. Ju, Q.; Tu, D.; Liu, Y.; Li, R.; Zhu, H.; Chen, J.; Chen, Z.; Huang, M.; Chen, X. Amine-Functionalized Lanthanide-Doped $KGdF_4$ Nanocrystals as Potential Optical/Magnetic Multimodal Bioprobes. *J. Am. Chem. Soc.* **2012**, *134*, 1323–1330.
42. Zeng, S.; Tsang, M.-K.; Chan, C.-F.; Wong, K.-L.; Hao, J. PEG Modified $BaGdF_5$:Yb/Er Nanoprobes for Multi-Modal Upconversion Fluorescent, *in Vivo* X-Ray Computed Tomography and Biomagnetic Imaging. *Biomaterials* **2012**, *33*, 9232–9238.
43. Grzyb, T.; Węcławiak, M.; Pędziński, T.; Lis, S. Synthesis, Spectroscopic and Structural Studies on YOF, LaOF and GdOF Nanocrystals Doped with Eu^{3+}, Synthesized *via* Stearic Acid Method. *Opt. Mater.* **2013**, *35*, 2226–2233.
44. Zhang, Y.; Geng, D. L.; Kang, X. J.; Shang, M. M.; Wu, Y.; Li, X. J.; Lian, H. Z.; Cheng, Z. Y.; Lin, J. Rapid, Large-Scale, Morphology-Controllable Synthesis of YOF:Ln^{3+} (Ln = Tb, Eu, Tm, Dy, Ho, Sm) Nano-/Microstructures with Multicolor-Tunable Emission Properties. *Inorg. Chem.* **2013**, *52*, 12986–12994.
45. Zhong, Y.; Tian, G.; Gu, Z.; Yang, Y.; Gu, L.; Zhao, Y.; Ma, Y.; Yao, J. Elimination of Photon Quenching by a Transition Layer to Fabricate a Quenching-Shield Sandwich Structure for 800 nm Excited Upconversion Luminescence of Nd^{3+}-Sensitized Nanoparticles. *Adv. Mater.* **2014**, *26*, 2831–2837.
46. Xia, L.; Kong, X.; Liu, X.; Tu, L.; Zhang, Y.; Chang, Y.; Liu, K.; Shen, D.; Zhao, H.; Zhang, H. An Upconversion Nanoparticle-Zinc Phthalocyanine Based Nanophotosensitizer for Photodynamic Therapy. *Biomaterials* **2014**, *35*, 4146–4156.
47. Carlos, L. D.; Ferreira, R. A. S.; Bermudez, V. d. Z.; Julian-Lopez, B.; Escribano, P. Progress on Lanthanide-Based Organic-Inorganic Hybrid Phosphors. *Chem. Soc. Rev.* **2011**, *40*, 536–549.
48. Hao, J.; Zhang, Y.; Wei, X. Electric-Induced Enhancement and Modulation of Upconversion Photoluminescence in Epitaxial $BaTiO_3$:Yb/Er Thin Films. *Angew. Chem., Int. Ed.* **2011**, *50*, 6876–6880.
49. Tu, D.; Liu, Y.; Zhu, H.; Li, R.; Liu, L.; Chen, X. Breakdown of Crystallographic Site Symmetry in Lanthanide-Doped $NaYF_4$ Crystals. *Angew. Chem., Int. Ed.* **2013**, *52*, 1128–1133.
50. Kim, J.; Piao, Y.; Hyeon, T. Multifunctional Nanostructured Materials for Multimodal Imaging, and Simultaneous Imaging and Therapy. *Chem. Soc. Rev.* **2009**, *38*, 372–390.
51. Glasbeek, M.; Zhang, H. Femtosecond Studies of Solvation and Intramolecular Configurational Dynamics of Fluorophores in Liquid Solution. *Chem. Rev.* **2004**, *104*, 1929–1954.
52. Zhao, J.; Sun, Y.; Kong, X.; Tian, L.; Wang, Y.; Tu, L.; Zhao, J.; Zhang, H. Controlled Synthesis, Formation Mechanism, and Great Enhancement of Red Upconversion Luminescence of $NaYF_4$:Yb^{3+},Er^{3+} Nanocrystals/Submicroplates at Low Doping Level. *J. Phys. Chem. B* **2008**, *112*, 15666–15672.
53. Wang, F.; Liu, X. Upconversion Multicolor Fine-Tuning: Visible to Near-Infrared Emission from Lanthanide-Doped $NaYF_4$ Nanoparticles. *J. Am. Chem. Soc.* **2008**, *130*, 5642–5643.
54. Wang, S.-S.; Chen, W.-T.; Li, Y.; Wang, J.; Sheu, H.-S.; Liu, R.-S. Neighboring-Cation Substitution Tuning of Photoluminescence by Remote-Controlled Activator in Phosphor Lattice. *J. Am. Chem. Soc.* **2013**, *135*, 12504–12507.
55. Wang, J.; Wang, F.; Wang, C.; Liu, Z.; Liu, X. Single-Band Upconversion Emission in Lanthanide-Doped $KMnF_3$ Nanocrystals. *Angew. Chem., Int. Ed.* **2011**, *50*, 10369–10372.

56. Yin, W.; Zhao, L.; Zhou, L.; Gu, Z.; Liu, X.; Tian, G.; Jin, S.; Yan, L.; Ren, W.; Xing, G.; *et al.* Enhanced Red Emission from GdF_3:Yb^{3+},Er^{3+} Upconversion Nanocrystals by Li^+ Doping and their Application for Bioimaging. *Chem.—Eur. J.* **2012**, *18*, 9239–9245.
57. Zeng, S.; Yi, Z.; Lu, W.; Qian, C.; Wang, H.; Rao, L.; Zeng, T.; Liu, H.; Liu, H.; Fei, B.; *et al.* Simultaneous Realization of Phase/Size Manipulation, Upconversion Luminescence Enhancement, and Blood Vessel Imaging in Multifunctional Nanoprobes through Transition Metal Mn^{2+} Doping. *Adv. Funct. Mater.* **2014**, *24*, 4051–4059.
58. Yang, D.; Kang, X.; Ma, P. A.; Dai, Y.; Hou, Z.; Cheng, Z.; Li, C.; Lin, J. Hollow Structured Upconversion Luminescent $NaYF_4$:Yb^{3+},Er^{3+} Nanospheres for Cell Imaging and Targeted Anti-Cancer Drug Delivery. *Biomaterials* **2013**, *34*, 1601–1612.
59. Wang, G.; Peng, Q.; Li, Y. Upconversion Luminescence of Monodisperse CaF_2:Yb^{3+}/Er^{3+} Nanocrystals. *J. Am. Chem. Soc.* **2009**, *131*, 14200–14201.
60. Zhao, J.; Lu, Z.; Yin, Y.; McRae, C.; Piper, J. A.; Dawes, J. M.; Jin, D.; Goldys, E. M. Upconversion Luminescence with Tunable Lifetime in $NaYF_4$:Yb,Er Nanocrystals: Role of Nanocrystal Size. *Nanoscale* **2013**, *5*, 944–952.
61. Lin, C.; Berry, M. T.; Anderson, R.; Smith, S.; May, P. S. Highly Luminescent NIR-to-Visible Up-conversion Thin Films and Monoliths Requiring No High-Temperature Treatment. *Chem. Mater.* **2009**, *21*, 3406–3413.
62. Tian, Q.; Hu, J.; Zhu, Y.; Zou, R.; Chen, Z.; Yang, S.; Li, R.; Su, Q.; Han, Y.; Liu, X. Sub-10 nm Fe_3O_4@$Cu_{2-x}S$ Core-Shell Nanoparticles for Dual-Modal Imaging and Photothermal Therapy. *J. Am. Chem. Soc.* **2013**, *135*, 8571–8577.
63. Gao, W.; Chan, J. M.; Farokhzad, O. C. pH-Responsive Nanoparticles for Drug Delivery. *Mol. Pharmaceutics* **2010**, *7*, 1913–1920.
64. Schrum, K. F.; Lancaster, J. M.; Johnston, S. E.; Gilman, S. D. Monitoring Electroosmotic Flow by Periodic Photobleaching of a Dilute, Neutral Fluorophore. *Anal. Chem.* **2000**, *72*, 4317–4321.
65. Petoral, R. M.; Söderlind, F.; Klasson, A.; Suska, A.; Fortin, M. A.; Abrikossova, N.; Selegård, L. A.; Käll, P.-O.; Engström, M.; Uvdal, K. Synthesis and Characterization of Tb^{3+}-Doped Gd_2O_3 Nanocrystals: A Bifunctional Material with Combined Fluorescent Labeling and MRI Contrast Agent Properties. *J. Phys. Chem. C* **2009**, *113*, 6913–6920.
66. Park, J. Y.; Baek, M. J.; Choi, E. S.; Woo, S.; Kim, J. H.; Kim, T. J.; Jung, J. C.; Chae, K. S.; Chang, Y.; Lee, G. H. Paramagnetic Ultrasmall Gadolinium Oxide Nanoparticles as Advanced T_1 MRI Contrast Agent: Account for Large Longitudinal Relaxivity, Optimal Particle Diameter, and *in Vivo* T_1 MR Images. *ACS Nano* **2009**, *3*, 3663–3669.
67. Stöber, W.; Fink, A.; Bohn, E. Controlled Growth of Monodisperse Silica Spheres in the Micro Size Range. *J. Colloid Interface Sci.* **1958**, *26*, 62–69.
68. Goyanes, S.; Rubiolo, G. R.; Salazar, A.; Jimeno, A.; Corcuera, M. A.; Mondragon, I. Carboxylation Treatment of Multiwalled Carbon Nanotubes Monitored by Infrared and Ultraviolet Spectroscoples and Scanning Probe Microscopy. *Diamond Relat. Mater.* **2007**, *16*, 412–417.
69. Wang, J.; Zhang, Z.; Zha, S.; Zhu, Y.; Wu, P.; Ehrenberg, B.; Chen, J.-Y. Carbon Nanodots Featuring Efficient FRET for Two-Photon Photodynamic Cancer Therapy with a Low Laser Power Density. *Biomaterials* **2014**, *35*, 9372–9381.
70. Jin, S.; Zhou, L.; Gu, Z.; Tian, G.; Yan, L.; Ren, W.; Yin, W.; Liu, X.; Zhang, X.; Hu, Z.; *et al.* A New Near Unfrared Photosensitizing Nanoplatform Containing Blue-Emitting Up-Conversion Nanoparticles and Hypocrellin for Photodynamic Therapy of Cancer Cells. *Nanoscale* **2013**, *5*, 11910–11918.